J. Fluid Mech. (2008), *vol.* 615, *pp.* 53–92.
doi:10.1017/S0022112008003601 Printed in the United Kingdom

Low-dimensional characteristics of a transonic jet. Part 2. Estimate and far-field prediction

C. E. TINNEY[1], L. S. UKEILEY[2] AND M. N. GLAUSER[3]

[1]Department of Aerospace Engineering & Engineering Mechanics, University of Texas at Austin, Austin, TX 78712, USA

[2]Department of Mechanical & Aerospace Engineering, University of Florida, Research and Engineering Education Facility, Shalimar, FL 32579, USA

[3]Department of Mechanical & Aerospace Engineering, Syracuse University, Syracuse, NY 13244, USA

(Received 14 June 2007 and in revised form 9 July 2008)

Complementary low-dimensional techniques are modified to estimate the most energetic turbulent features of a Mach 0.85 axisymmetric jet in the flow's near-field regions via spectral linear stochastic estimation. This model estimate is three-dimensional, comprises all three components of the velocity field and is time resolved. The technique employs the pressure field as the unconditional input, measured within the hydrodynamic periphery of the jet flow where signatures (pressure) are known to comprise a reasonable footprint of the turbulent large-scale structure. Spectral estimation coefficients are derived from the joint second-order statistics between coefficients that are representative of the low-order pressure field (Fourier-azimuthal decomposition) and of the low-order velocity field (proper orthogonal decomposition). A bursting-like event is observed in the low-dimensional estimate and is similar to what was found in the low-speed jet studies of others. A number of low-dimensional estimates are created using different velocity–pressure mode combinations from which predictions of the far-field acoustics are invoked using Lighthill's analogy. The overall sound pressure level (OASPL) directivity is determined from the far-field prediction, which comprises qualitatively similar trends when compared to direct measurements at $r/D = 75$. Retarded time topologies of the predicted field at 90° and 30° are also shown to manifest, respectively, high- and low-frequency wave-like motions when using a combination of only the low-order velocity modes ($m = 0, 1, 2$). This work thus constitutes a first step in developing low-dimensional and dynamical system models from hydrodynamic pressure signatures for estimating and predicting the behaviour of the energy-containing events that govern many of the physical constituents of turbulent flows.

1. Introduction

Capturing both the spatial and temporal features of the fully three-dimensional turbulent structure is one of many challenges in studying the physical mechanisms in turbulent flows. With the recent technology boom in the computing industry during the turn of the twenty-first century, the ability to reproduce both the spatial and temporal features of turbulent flows has become more promising, both experimentally and numerically. In the experimental community, recent advancements have moved from not only higher-resolution time-independent planar optical systems (PIV) (Adrian

1991; Raffel, Willert & Kompenhans 1998), but to time-resolved planar optical systems (TR-PIV) (Wernet 2006), and even holographic and tomographic PIV systems (Pu, Song & Meng 2000; Pan & Meng 2002; Elsinga *et al.* 2006) which allow for a full volume of fluid flow to be captured and quantified. Though there are still many challenges facing the experimentalist (compromises between laser power, the dimensions of the spatial window / resolution and sampling speed) the progression in the development of these resources has provided a glimpse into the future capabilities of these technologies as we continue to address outstanding questions in fluid and thermal related sciences.

Complementary to these technological advancements, extensive work has been done in the past two decades using low-order dynamical systems models (LODS). One approach which has shown remarkable accomplishments and innovation uses both experimental and numerical databases (Aubry *et al.* 1988; Glauser, Zheng & Doering 1991; Rempfer 2000; Ukeiley *et al.* 2001; Gordeyev & Thomas 2002; Noack *et al.* 2003; Rowley, Colonius & Murray 2004; Bergmann, Cordier & Brancher 2005; Perret, Collin & Delville 2006). It begins with the premise that the first few most energetic modes (obtained via proper orthogonal decomposition), in a turbulent field that encompasses an infinite number of modes, constitute a moderate to large percentage of the turbulent kinetic energy and are responsible for many of the physical mechanisms governing, e.g. heat, mass and momentum transfer, spreading and mixing. Thus, at the forefront of the LODS model, we rely on a mathematical tool, the proper orthogonal decomposition (POD), to systematically quantify the energy of the various mode constituents that are a manifestation of the turbulence. In doing so the most energetic features of the flow (modes associated with the more energetic large-scale events) are separated from the underlying turbulence (less energetic events) in order to study the evolution of the former in space and time.

A common approach for constructing LODS models is through a Galerkin projection of the Navier–Stokes equations onto the POD basis from which time-resolved POD expansion coefficients are obtained (Aubry *et al.* 1988; Ukeiley *et al.* 2001). Subtle differences do, however, exist between the numerical and experimental community's interests in these models. To some degree, the numerical undertaking of this approach is simply to reduce the complexity of the flow model into a set of mathematical or empirical modes that can provide an efficient representation of the flow dynamics, whereas the experimental undertaking relies on the model system to insert a time dependence into the expansion coefficients, both of which aim to understand the key physical processes that govern the overall system. The success of these Galerkin models requires an appropriate system of governing flow equations (e.g. full or linearized Navier–Stokes, compressible, incompressible) that are accurate representations of the flow dynamics, considering the boundary conditions of the model and the stability of the truncated system of equations. In turn, the LODS model becomes a complete representation of the low-order spatial flow dynamics through a balance of the governing flow equations. (It is worth pointing out that LODS models are often only valid over fixed values of the flow parameters, e.g. Reynolds number or Mach number.) Alternatively, time-resolved expansion coefficients (e.g. from stationary and statistically independent data sets such as PIV), can be obtained by other means which we will discuss here as it pertains to the choice of low-dimensional tools that are implemented in this analysis.

An increasingly popular alternative method for obtaining time-resolved POD expansion coefficients for constructing low-dimensional models is through the stochastic estimation techniques of Adrian (1977, 1991). The outline for this process

was originally presented by Ukeiley, Cole & Glauser (1993) and further refined by Bonnet *et al.* (1994). The latter employed an unconditional estimate of the raw velocity field in a two-dimensional subsonic mixing layer via linear stochastic estimation (LSE), followed by a low-dimensional description of the model estimate via POD. Since then, the joint implementation of these analysis tools (POD and LSE) have taken many different forms in the experimental community using a variety of different flows (backward facing ramps (Taylor & Glauser 2004), axisymmetric sudden expansions (Tinney *et al.* 2002), axisymmetric backward facing steps (Hudy, Naguib & Humphreys 2007) plane mixing layers (Druault, Delville & Bonnet 2005), cavity flows (Murray & Ukeiley 2006), axisymmetric jet flows (Ewing & Citriniti 1999; Picard & Delville 2000; Taylor, Ukeiley & Glauser 2001; Tinney *et al.* 2005, 2006; Iqbal & Thomas 2007), pressure fields in the periphery of axisymmetric jets (Coiffet *et al.* 2004), wall jets (Hall & Ewing 2006) and incipiently separated airfoils (Glauser *et al.* 2004; Pinier *et al.* 2007)).

Many of the deviations to these complementary techniques have been driven principally by the design architecture of the experiment, the type of flow behaviour studied and the instrument's diagnostics. Thus, where the time dependence of the POD expansion coefficients are concerned, the alternatives to the original methods proposed by Bonnet *et al.* (1994) have been developed not only to insert (by means of stochastic estimation) the necessary temporal resolution for producing time-varying expansion coefficients, but to improve the correlation that links the unconditional events to the event being estimated. The latter is known to improve the accuracy of the model estimate. To this end, a subset of these approaches have used the pressure field (Picard & Delville 2000; Taylor & Glauser 2004; Coiffet *et al.* 2004; Glauser *et al.* 2004; Tinney *et al.* 2005; Hall & Ewing 2006; Hudy *et al.* 2007; Ukeiley *et al.* 2007) for reasons that are discussed as it pertains to unbounded turbulent jet flows.

Foremost, where aeroacoustic sources of noise are concerned, the pressure field, within the periphery of the jet flow, comprises a superposition of both hydrodynamic (non-propagating) and acoustic (propagative) fluctuations (Arndt, Long & Glauser 1997; Coiffet *et al.* 2006), therefore offering a unique opportunity to study the two forms *in situ*. Secondly, the hydrodynamic pressure fluctuations are known to carry a convective footprint of the large-scale coherent structure (Lau, Fisher & Fuchs 1972; Petersen 1978; Chang 1985; Arndt, Long & Glauser 1997; (Picard & Delville 2000; Ukeiley & Ponton 2004; Hall, Glauser & Tinney 2005; Coiffet *et al.* 2006; Tinney *et al.* 2007). These hydrodynamic signatures, characterized by a $kr^{-20/3}$ decay law (Arndt, Long & Glauser 1997), offer a nonintrusive means by which to sense the flow dynamics of the large-scale structure, which for practical feedback control strategies, are the only events that can arguably be controlled. Furthermore, for applications, commercially available pressure transducers are relatively robust instruments that require comparatively little effort in their installation and calibration, and are typically capable of resolving all of the necessary time scales that are of interest. There are, however, certain qualities concerning the implementation of pressure fluctuations as an input for obtaining the time-varying expansion coefficients for a low-dimensional estimate, as we will now consider.

Batchelor (1951) proposed one of the first simplified models for relating the mean square velocity fluctuations in high-Reynolds-number isotropic incompressible turbulence to the mean square pressure fluctuations (over a range of spatial positions) using an empirically derived constant and a characteristic velocity correlation function. George, Beuther & Arndt (1984) separated the unsteady Poisson equation into its linear (shear-noise) and quadratic (self-noise) terms to show that the shear-noise terms

(turbulence-mean-shear) dominated the energy-containing range of the turbulence spectrum with a spectral decay law of $k^{-11/3}$ in the inertial subrange. Consequently, the self-noise terms (turbulence–turbulence) dominated the high-wavenumber range of the spectrum with a spectral decay of $k^{-7/3}$. Overall, the spectral decay rates for the pressure field were shown to be uniquely different from the velocity field ($k^{-5/3}$), thus demonstrating how the pressure field acts as a natural wave-like filter. To this end, artefacts of the pressure field's filtering characteristics had already been observed in a number of other studies. Michalke & Fuchs (1975) showed that the axial component of velocity in a round jet (at $r/D = 0.5, x/D = 3$) comprised higher Fourier-azimuthal mode number behaviours with peak energies in mode 5, complementary to several more recent undertakings (Glauser 1987; Glauser & George 1987; Ukeiley, Seiner & Ponton 1999; Citriniti & George 2000; Jung, Gamard & George 2004; Tinney *et al.* 2008). Contrary to the velocity fluctuations, surveys of pressure fluctuations by Michalke & Fuchs (1975) at the same axial and radial position exhibited much lower azimuthal-mode-number behaviours with prominent energies manifest in modes $0, 1, 2$ and 3. Michalke & Fuchs (1975) concluded from this that the axisymmetric ring vortex structure was the most efficient source of far-field sound. Since then, the rapid roll-off of the pressure spectra (George *et al.* 1984) and the stark differences between the Fourier-azimuthal behaviours of the pressure and velocity fluctuations (Michalke & Fuchs 1975; Arndt, Long & Glauser 1997; Tinney *et al.* 2007) within the hydrodynamic periphery of the jet has provided an *a priori* understanding that the pressure field is driven principally by the large turbulent scales of the flow. This, of course, possesses certain strengths and weaknesses concerning the pressure field as an input for obtaining time-varying POD expansion coefficients for generating a low-dimensional estimate of the flow dynamic. To some degree, we can anticipate only a handful of turbulent modes to be included in the low-dimensional estimate, subsequent to the natural filtering effects from the pressure field, rather than a selection based on the turbulent kinetic energy of the flow (which we would choose to extract via POD).

We will thus focus on two primary objectives in this paper. We first endeavour to improve on existing methodologies for constructing a low-dimensional estimate of a turbulent flow (high-subsonic high-Reynolds-number axisymmetric jet) through a spectral (multi-time) stochastic estimate of the time-varying POD expansion coefficients. We seek to do so by coupling the pressure field: situated in the periphery of the jet, with the velocity field: surveyed in the growth and early saturation regions of the flow. The analysis is unique in that both the pressure and velocity fields are reduced to their low-order coefficients (Fourier-azimuthal and POD, respectively), from which spectral estimation coefficients are obtained via a calculation of their joint second-order statistics. (Aside from subtle differences in our theoretical design, the extended-POD technique proposed by Borée (2003) has close proximity to the current analytical recipe for producing time-varying coefficients from the joint second-order statistics between the low-order coefficients of interrelated quantities that exist within the same sub-domain.) In doing so, a second objective is established: to reveal the mechanisms in the fluctuating velocity that are responsible for driving the pressure field located within the hydrodynamic periphery of the jet.

Although there are different ways in which the analysis techniques for this low-dimensional estimate may be derived, they are here presented in a form that is tailored to the design of this experiment, the arrangement and characteristics of the instruments employed and to the objectives that we seek to accomplish. When appropriate, we will identify improvements to these techniques to be used at a later stage in this greater

effort towards developing a low-dimensional estimate for subsequent identification and feedback control of the sound sources from high-speed turbulent jets and for many other practical engineering problems in turbulence.

The outline of the paper is as follows. A brief description of the experiment and instrumentation are provided in § 2, including a statistical characterization of the pressure array (this was not described in Part 1, Tinney, Glauser & Ukeiley 2008). In § 3, we will provide the mathematical recipe for creating the low-dimensional estimate of the flow using a modified form of the complementary techniques described by Ukeiley, Cole & Glauser (1993) and Bonnet *et al.* (1994). Concerns regarding the linear truncation of this approach will also be addressed. A discussion involving the low-order coupling of the velocity modes with the pressure modes will be provided in § 4, followed by an interpretation of the low-dimensional estimate in § 5. In § 6, the acoustic source field is calculated from the model and an attempt is made to predict the far-field pressure at various observer positions using Lighthill's (1952) analogy. Concluding remarks are provided in § 7 along with provisions for improving the current research approach.

2. Facility, instrumentation and flow conditions

2.1. *The near-field velocity*

The experiments were conducted at Syracuse University's 206 m^3 fully anechoic chamber, the highlights of which are discussed in Tinney *et al.* (2004). The principal measurements presented here will comprise an unheated jet exiting from a converging axisymmetric nozzle with a centreline exit velocity U_j corresponding to a nominal Mach number of 0.85 ($Re_D = 1 \times 10^6$). The nozzle diameter is $D = 50.8$ mm and the flow exits into a quiescent environment with temperatures around (283° K). Measurements of the near-field velocity were performed in the (r, θ)-plane of the jet at discrete streamwise locations between $x/D = 3.0$ and 8.0 ($\Delta x/D = 0.25$) using a Dantec Dynamics stereo (three-component) particle image velocimetry (PIV) system. Single-point mean velocity and turbulence statistics were obtained from an ensemble average of 1250 statistically independent PIV measurements at each axial station in the flow and were shown in Part 1 to compare well with the PIV measurements of Arakeri *et al.* (2003) and Alkislar, Krothapalli & Butler (2007), and more qualitatively with the low-speed jet measurements of Bradshaw, Ferriss & Johnson (1964), Lau, Morris & Fisher (1979), Hussain & Clark (1981) and Jung *et al.* 2004. For a description of the PIV arrangement, as well as the processing of the PIV data (grid transformation of the PIV vector maps, the jet's turbulent statistics, preservation of the momentum integral, spatial filtering effects), see Part 1, § 2.

2.2. *The near-field pressure*

The principle near-field pressure measurements comprised an azimuthal array of 15 Kulite XCE-093 model, 35 kPa gauge pressure transducers, equidistantly separated by $\Delta\theta = 24°$. The transducers are rear vented with a 2.36 mm diameter body, a nominal sensitivity of 2.9 μV Pa^{-1} and a dynamic response range up to 50 kHz. These transducers are compensated for exposure to temperatures up to 550° K with little shift in their response functions. Excitation and amplification for these instruments were provided by several model-136 Endevco signal conditioners comprising a 200 kHz bandwidth, programmable gains and built-in four-pole Butterworth low-pass filters. A National Instruments PXI system digitized the signals from the Endevco units and

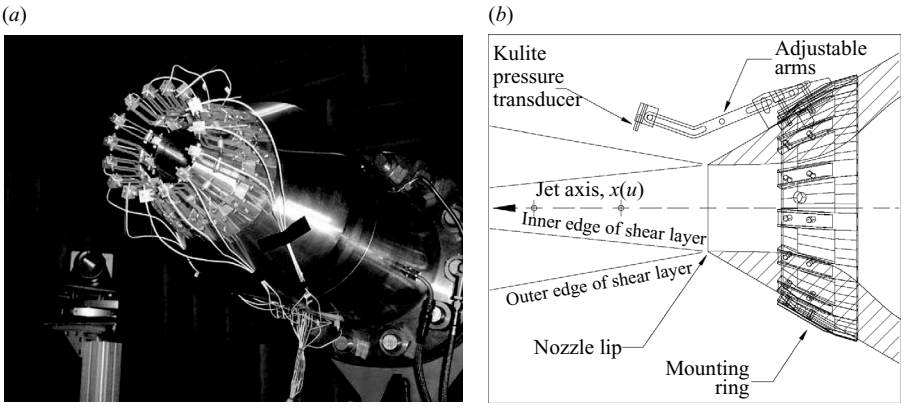

FIGURE 1. (*a*) *In situ* and (*b*) schematic layout of the probe holder used to support an azimuthal array of 15 Kulite pressure transducers at $x/D = r/D = 0.875$.

were equipped with two NI-4472 boards. Each board contains 8 single and differential ended channels with 24-bit resolution, anti-aliasing filters, and a maximum sampling rate (per channel) of 102.4 kHz. The sampling frequency (f_s) of the transducers was set at 30 kHz.

Several preliminary experiments were performed in a Mach 0.60 jet using a 1/4 in. B&K type-4135 microphone in the (r, x)-plane of the jet's near-field pressure region to assess the sensitivity of the measurement field outside the turbulent shear layer between $x/D = 0.25$ and 0.75 and $r/D = 0.7$ and 1.1. This concerted effort was used as a guide for positioning the azimuthal array of Kulite transducers so as to capture a reasonable signature of the hydrodynamic pressure field for the Mach 0.85 jet experiments. A discussion pertaining to a subset of these results at Mach 0.60 using the 1/4 in. B&K microphone is provided in Tinney *et al.* (2007). Based on these measurements, the azimuthal array of Kulite transducers was placed in the periphery of the jet shear layer at $x/D = r/D = 0.875$ and supported by a probe holder (figure 1) that was located behind the nozzle exit plane in order to reduce the intrusiveness of these instruments on the jet shear layer.

Following the analysis of Arndt *et al.* (1997), the pressure wavenumber spectra was determined using the Mach 0.85 pressure data from which the hydrodynamic ($kr_s^{-6.67}$) and acoustic signatures (kr_s^{-2}) are shown in figure 2(*a*). Here, r_s, ρ and k denote the radial distance outward from the centre of the shear layer at $r/D \sim 0.5$, the density of the quiescent fluid, and the wavenumber, respectively. The behaviour of the wavenumber spectra found in this study is similar to the findings from other axisymmetric jet flows reported by Arndt *et al.* (1997) and Coiffet *et al.* (2006). It should be pointed out that the first attempt at acquiring a signature of the hydrodynamic footprint of the jet structure comprised an azimuthal arrangement of transducers at the jet lip ($x/D = 0$, $r/D = 0.5$). The results of this produced a flat spectrum, contrary to the one shown in figure 2(*a*), and no correlation with the velocity field (both PIV and LDA surveys). An explanation of this is provided in the discussion of Ko & Davies (1971) as it pertains to the roll-up structure of the jet which occurs around one jet diameter downstream from the nozzle exit. Thus, after the first half-diameter ($x/D > 0.5$), the hydrodynamic signatures are reminiscent of the first roll-up structure, before which ($x/D \leqslant 0.25$) the signatures are either very weak or non-existent. Ko & Davies (1971) found that this was consistently the case

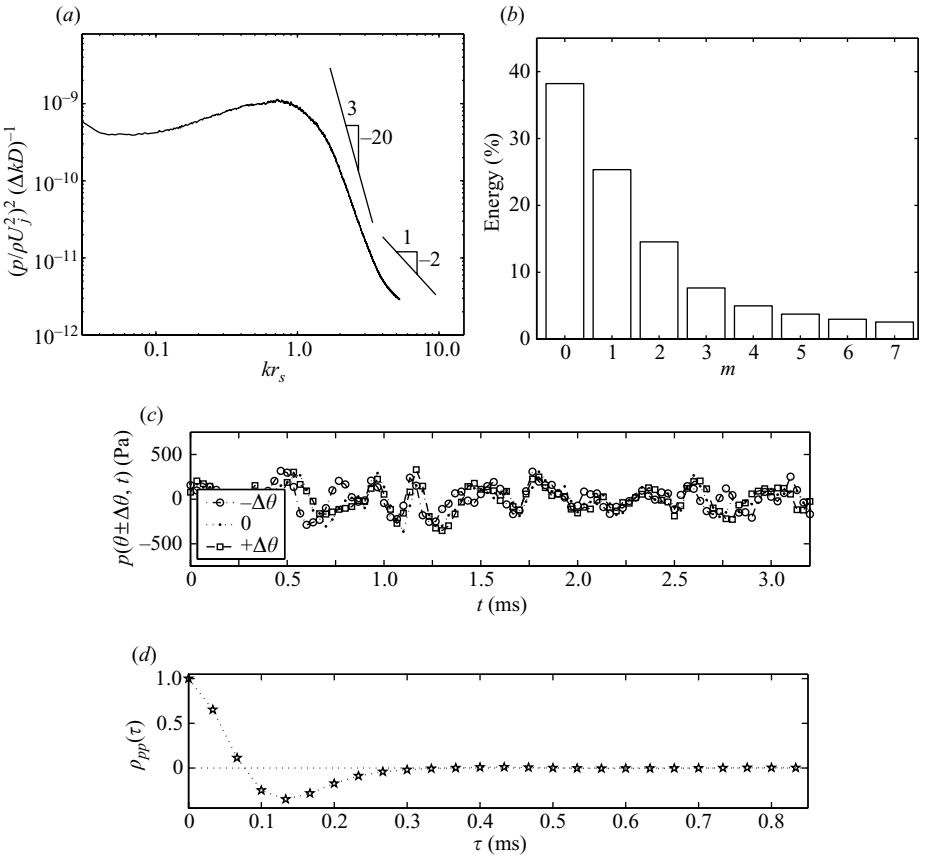

FIGURE 2. (*a*) Pressure wavenumber spectra. (*b*) Averaged Fourier-azimuthal eigenspectra. (*c*) Sample time series of three successive transducers. (*d*) Normalized Eulerian temporal correlation function.

for the Mach-number range investigated (between 0.015 and 0.4) and appears to extend up to the Mach 0.85 case we are studying here.

As the pressure transducers were fixed along an azimuthal array, a Fourier-azimuthal decomposition (ensemble averaged) was performed, the results of which are shown in figure 2(*b*) normalized by the energy of the half-spectrum. The results are obtained after azimuthal averaging using different transducers to define where $\theta = 0$. The variation between different starting points was within 10 % of the mean value and demonstrated a small misalignment of the azimuthal array with respect to the jet axis. Alignment is not a concern with the analytical techniques that are employed in the subsequent discussion. The simplicity of the Fourier-azimuthal modes are similar to the constituents of Michalke & Fuchs (1975) and are complementary to the azimuthal spatial correlations of Ukeiley & Ponton (2004). Although the measurements in the current investigation are confined to a fixed region in space near the nozzle exit plane, Coiffet *et al.* (2004) has shown that the Fourier-azimuthal characteristics of the pressure signatures in the near-field surrounding the turbulent jet are fairly independent of axial position. (This conclusion is drawn from near-field pressure measurements performed within the first six diameters of a Mach 0.30 jet, though it is plausible that the azimuthal eigenspectra will remain unchanged into

the transition and far-field regions of the jet.) The peak Strouhal number of the near-field pressure is, however, influenced by the axial station where measurements are performed and will be important to the selection of an appropriate conditional estimation technique to be discussed in § 3.2.

A sample time series is shown in figure 2(*c*) using three successive transducers. Considering the Fourier-azimuthal eigenspectra, the raw pressure–time series manifest signatures from well-organized azimuthally coherent events, similarly demonstrated by Petersen (1978). A calculation of the Eulerian temporal correlation function is shown in figure 2(*d*) with a peak Strouhal number of $St_D = fD/U_j \sim 0.45$ determined from this location in the flow. Although the current investigation comprises pressure measurements that share many similarities with the analysis presented by Arndt *et al.* (1997) and Coiffet *et al.* (2006), the focus of this study is towards building a low-dimensional estimate of this high-subsonic high-Reynolds-number jet flow using these pressure signatures, obtained near the nozzle exit, as the time-dependent input for the estimate. Thus, the aforementioned studies have been considered only briefly to demonstrate the quality of the pressure measurements acquired for this analysis, and the similarity of these measurements to others that have been reported in the literature.

2.3. *Synchronization of measurements*

To relate the fluctuating pressure signatures, sampled on a fixed array in the periphery of the jet flow, to the turbulent velocity field, traversed along various axial stations, a trigger pulse from the PIV system's first laser was sampled synchronously with the PXI system (1250 paired laser pulses at each axial station). Thus, for a given axial positioning of the PIV laser sheet, 1250 total trigger pulses were recorded along with 15 channels of continuous pressure. We will revisit this in a later part of the discussion as it implicates the procedure for estimating the velocity field.

3. Low-dimensional analysis tools

3.1. *Proper orthogonal decomposition*

A proper orthogonal decomposition (Lumley 1967, 1981; Glauser, Leib & George 1985; Berkooz, Holmes & Lumley 1993) was performed on the fluctuating velocity (ensemble-averaged mean velocity removed) at each discrete axial station that the PIV system was traversed to. The application of the POD to the current study is described in greater detail in Part 1, where both scalar and vector forms of the technique were applied to the PIV data set. Since the source field in Lighthill's (1952) acoustic analogy uses terms such as $\partial u_i/\partial x_j$, where $i, j = 1, 2, 3$, or in the vortex–noise analogies of Möhring (1978) and Powell (1964) which comprises gradients of the vorticity field, the low-dimensional features of all three velocity components are essential in this analysis. The full (time suppressed) vector form of the integral eigenvalue problem of the POD is,

$$\int_R B_{ij}(r, r', x; m)\Phi_j^{(n)}(r', x; m)r'\mathrm{d}r' = \Lambda^{(n)}(x; m)\Phi_i^{(n)}(r, x; m), \tag{3.1}$$

and is necessary for establishing a nomenclature for the subsequent analysis to be referred to. Φ and Λ are the empirically derived eigenfunctions and eigenvalues, respectively, while the kernel $B_{ij}(r, r', x; m)$ used in the maximization comprises a

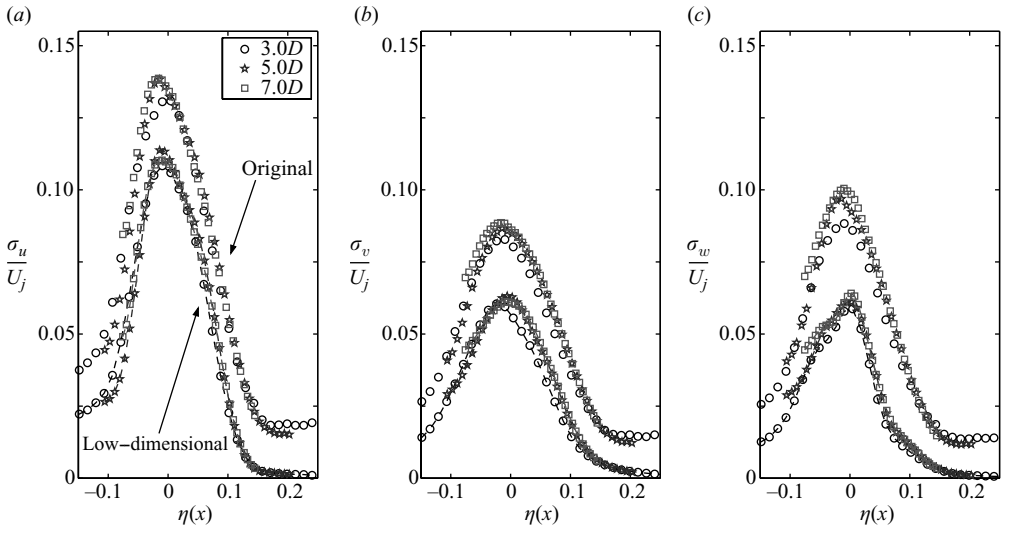

FIGURE 3. Turbulence velocity ratios obtained from the raw measurements (symbols) of the (*a*) axial and (*b*) radial and (*c*) azimuthal velocity components compared with the low-ordered reconstructions (symbols with dashed lines) using Fourier-azimuthal modes $m=0$ to 11 and POD modes $n=1+2$. The abscissa axis labelling is defined as $\eta(x)=(r-r_{0.5})/x$.

Fourier-azimuthal transformed ($\vartheta \rightarrow m$), two-point velocity cross-correlation tensor,

$$B_{ij}(r, r', x; m) = \frac{1}{2\pi}\int_{-\pi}^{\pi} R_{ij}(r, r', \vartheta, x)\mathrm{e}^{-\mathrm{i}m\vartheta}\,\mathrm{d}\vartheta, \tag{3.2}$$

as is typically done with flows that are azimuthal invariant in their averaged statistical properties. The cross-correlation tensor was created using all nine normal- and shear-stress components and was generated by ensemble averaging over 1250 statistically independent PIV snap-shots of the flow acquired at each of the 21 axial stations studied,

$$R_{ij}(r, r', \vartheta, x) = \langle u_i(r, \theta, x, t_s)u_j(r', \theta+\vartheta, x, t_s)\rangle. \tag{3.3}$$

As the POD eigenfunctions represent an ordered sequence of optimized spatial functions (comprising more energy per mode than any other linear expansion), they can be used to reconstruct the Fourier transformed kernel in (3.2) as follows:

$$\mathscr{B}_{ij}^{(k)}(r, r', x; m) = \sum_{n=1}^{k} \Lambda^{(n)}(x; m)\Phi_i^{(n)}(r, x; m)\Phi_j^{(n)*}(r', x; m), \tag{3.4}$$

where $\mathscr{B}_{ij}^{(k)}(r, r', x; m) = B_{ij}(r, r', x; m)$ for $k = cN$, and $(^*)$ denotes the complex conjugate. c represents the number of components used in the vector application ($c=3$) and N is the number of points that were measured in r ($N=38$). In figure 3, the original turbulence profiles obtained from $\sigma_i = \sqrt{R_{ii}(r, r, \vartheta=0, x)}$, are shown alongside a low-dimensional reconstruction of the kernel using the most energetic Fourier-azimuthal modes $m=0$ to 11 and POD modes $n=1+2$ of the flow. The low-dimensional kernel has been inverse Fourier transformed ($m \rightarrow \vartheta$) and is shown here as the square root of the diagonal part of the matrix where $i=j$ and $r=r'$. These profiles are plotted using the similarity variable: $\eta(x)=(r-r_{0.5})/x$, where $r_{0.5}$ is the radial location where the mean velocity is 50 % of the jet exit velocity. It is

clear that the general shapes of the original profiles (25 % of the original energy) have been preserved using only a small fraction of the total number of modes (less than 1%).

For this analysis, we will concern ourselves with the eigenfunctions obtained from both the scalar and vector forms of the POD technique. The reasoning for this is two-fold. We first seek to understand the mechanisms responsible for driving the pressure field in the periphery of the jet, and to do so by analysing each component of the velocity field independently (in terms of its low-order coefficients) as obtained from the scalar form of the analysis tools. This is motivated by the investigation of Lau *et al.* (1972) who developed and experimentally verified a working model that described the relationship between the fluctuating near-field pressure in unbounded turbulence and its dependence on the axial and radial components of the fluctuating velocity. Secondly, where a temporal estimate of the low-order velocity coefficients are concerned, the vector form of the POD technique will be implemented as it ensures orthogonality between the empirical eigenfunctions comprising the various components of the velocity field. In the discussion to follow, it is therefore necessary to distinguish the solutions and functions comprising the scalar and vector forms of the techniques. Thus, where appropriate, we will resort to upper and lower case lettering, e.g. (Φ, Λ) versus (ϕ, λ), for those terms that relate to the vector and scalar application of (3.1), respectively.

Because of the PIV instrument's characteristics, time is a statistically independent realization (t_s) rather than a continuous function (t). Thus, it is not possible to reconstruct a time-dependent low-dimensional picture of this jet flow without additional work. This, of course, is one of the limitations of the selected instrument (PIV), whereby temporal resolution was compromised for spatial resolution. Therefore, we will insert time-dependent information into the flow from a linear stochastic estimate of the time-varying POD expansion coefficients using the time-dependent pressure fluctuations as the conditioning function. As we have discussed in § 1, this mathematical recipe falls within the genre of the methods developed by Ukeiley *et al.* (1993) and Bonnet *et al.* (1994). However, this recipe is modified to improve not only the strength of the joint second-order statistics between the pressure and velocity fields, but the accuracy of the characteristic time scales of the final event estimate by incorporating a combination of multi-time estimation techniques (Ewing & Citriniti 1999) and the extended POD (Borée 2003).

3.2. *Complementary techniques*

The basis for creating low-dimensional estimates originally comprises the linear stochastic estimation technique (LSE) of Adrian (1977, 1996) whereby the conditional average $\grave{u}(\boldsymbol{x}', t) = \langle u(\boldsymbol{x}', t) | u(\boldsymbol{x}, t) \rangle$, is known to provide the best mean square estimate of the fluctuation at position $\boldsymbol{x}'$ based on the fluctuation at position $\boldsymbol{x}$ at the same instant (the backwards slash $\grave{u}$ is here used to represent the estimated event). In this particular analysis of the Mach 0.85 jet, a spectral form of the stochastic methods will be used. This multi-time estimate was originally introduced by Ewing & Citriniti (1999) to study the topology of the axisymmetric jet's low-order structure and has been recently dubbed spectral linear stochastic estimation (SLSE) by Tinney *et al.* (2006). The SLSE was shown to improve on the accuracy of the conventional LSE methods when differences existed between the spectral characteristics of the conditioning event and the event being estimated. This is typically the case when large spatial separations (in the direction of a convecting frame of reference) exist between the grids comprising the conditioning field (input) and the estimated field (output). This SLSE procedure

yields the following estimate for $a(\boldsymbol{x}'; f)$ (see equation (8) of Ewing & Citriniti 1999), given the frequency dependent pressure $p_j(f)$,

$$\grave{a}(\boldsymbol{x}'; f) = b_j(\boldsymbol{x}'; f)p_j(f), \tag{3.5}$$

where the summation is performed over j conditioning events. Values for the estimation coefficients $b_j(\boldsymbol{x}'; f)$ are chosen such that the mean square error between the original and estimated field is minimized (Adrian 1977). This reduces to a linear system of equations from which the spectral estimation coefficients are obtained,

$$\langle p_j(f)p_k^*(f)\rangle b_j(\boldsymbol{x}'; f) = \langle a(\boldsymbol{x}'; f)p_k^*(f)\rangle. \tag{3.6}$$

In the present investigation, the pressure signatures, surveyed within the hydrodynamic near-field regions of the Mach 0.85 jet flow, are used as the conditioning events since they are known to carry a reasonable footprint of the most energetic features of the flow. Since the transducers were located in the periphery of the jet's shear layer, they are non-intrusive to the flow field, thus permitting a survey of the far-field acoustics to be synchronized with the near-field pressure/velocity field measurements. The recipe for creating the low-dimensional model estimate is given below.

The velocity field

The two-point Reynolds stress matrix $R_{ij}(r, r', \vartheta, x)$, comprising all nine normal and shear stress terms, is constructed from (3.3) using the statistically independent PIV surveys of the jet at 21 discrete axial stations in the flow.

A Fourier-azimuthal decomposition of the Reynolds stress matrix $(\vartheta \rightarrow m)$ is performed using (3.2) at each radial and axial position, and the integral eigenvalue problem of (3.1) is solved from which the empirical eigenvalues $\Lambda^{(n)}(x; m)$ and eigenfunctions $\Phi_i^{(n)}(r, x; m)$ are obtained.

Since the kernel reflects the mean statistical features of the turbulent jet, the POD eigenfunctions are used to reconstruct an instantaneous picture of the most energetic low-order modes (see § 5 of Part 1), using random and uncorrelated expansion coefficients,

$$a^{(n)}(x, t_s; m) = \int_R u_i(r, x, t_s; m)\Phi_i^{(n)*}(r, x; m)r\,\mathrm{d}r. \tag{3.7}$$

The pressure field

Similar to the velocity field, the pressure field is reduced to its low-order coefficients using Fourier expansions in azimuth and time (since POD reduces to a harmonic decomposition for periodic, homogenous, or stationary systems, the formulation using Fourier is effectively the same as that which uses POD). This is performed in a variety of steps starting with a single (azimuthal mode number and time) and double (azimuthal mode number and frequency) transformation of the instantaneous pressure,

$$p(t; m) = \frac{1}{2\pi}\int_{-\pi}^{\pi} p(t, \vartheta)\mathrm{e}^{-\mathrm{i}m\vartheta}\,\mathrm{d}\vartheta, \tag{3.8}$$

$$p(f, m) = \frac{1}{2\pi}\int_{-\infty}^{\infty}\int_{-\pi}^{\pi} p(t, \vartheta)\mathrm{e}^{-\mathrm{i}(2\pi f t + m\vartheta)}\mathrm{d}t\,\mathrm{d}\vartheta, \tag{3.9}$$

followed by an ensemble-averaged Fourier-azimuthal mode number cross-spectra,

$$S_{pp}(f,m)=\frac{1}{2\pi}\int_{-\infty}^{\infty}\int_{-\pi}^{\pi}\langle p(t,\theta)p(t+\tau,\theta+\vartheta)\rangle \mathrm{e}^{-\mathrm{i}(2\pi f\tau+m\vartheta)}\mathrm{d}\tau\,\mathrm{d}\vartheta. \tag{3.10}$$

Equations (3.8) to (3.10) are here defined separately as they are each part of the necessary ingredients for creating the low-dimensional estimate.

Linear stochastic estimation

A linear stochastic estimation is then performed which directly links the mode coefficients that are representative of the pressure field (azimuthally decomposed Fourier pressure modes) to the mode coefficients that are representative of the velocity field (POD velocity modes), that is $p(t;m) \leftrightarrows a^{(n)}(x,t_s;m)$ using spectral estimation coefficients. Recalling that the expansion coefficients are orthogonal and uncorrelated, and that their mean square values are the eigenvalues themselves, the following relationships can be written for the low-order coefficients of the velocity and pressure fields, respectively, as,

$$\langle a^{(n)}(x,t_s;m)a^{(\alpha)*}(x,t_s;\beta)\rangle\delta_{(n,\alpha)}\delta_{(m,\beta)}=\Lambda^{(n)}(x;m), \tag{3.11}$$

$$\langle p(t;m)p^{*}(t;\beta)\rangle\delta_{(m,\beta)}=B_{pp}(m), \tag{3.12}$$

where δ is the Kronecker delta, n and α represent POD mode numbers, m and β represent Fourier-azimuthal mode numbers, and the conjugation indicates Fourier phase shifts in azimuth. Thus, in view of (3.11) and (3.12), a simplification to the system of equations is obtained by truncating orthogonal and non-correlating modes, that is, the pressure modes that are orthogonal to the velocity modes. In doing so, only non-orthogonal modes are retained in the analysis,

$$R_{pa}^{(n)}(x,-\tau;m)=\langle p^{*}(t_s-\tau;m)a^{(n)}(x,t_s;\beta)\rangle\delta_{(m,\beta)}. \tag{3.13}$$

In (3.13), and for the remainder of the discussion, the notation for the pressure modes reflects the instant in time when the velocity field was 'frozen' and quantified by the PIV system. It was therefore some time period before $(t_s-\tau)$ when these same events, as captured by the PIV system, were sensed by the pressure array near the nozzle exit.

A cross-spectral correlation matrix is then generated comprising the POD expansion coefficients from the velocity measurements (3.7), the Fourier-azimuthal / time-dependent pressure coefficients (3.8) and the simplification of (3.13) as follows,

$$\begin{aligned}S_{pa}^{(n)}(x;-f,m)&=\frac{1}{2\pi}\int_{-\infty}^{\infty}\langle p^{*}(t_s-\tau;m)a^{(n)}(x,t_s;\beta)\rangle\delta_{(m,\beta)}\mathrm{e}^{\mathrm{i}2\pi f\tau}\mathrm{d}\tau\\&=\frac{1}{2\pi}\int_{-\infty}^{\infty}R_{pa}^{(n)}(x,-\tau;m)\mathrm{e}^{\mathrm{i}2\pi f\tau}\mathrm{d}\tau.\end{aligned} \tag{3.14}$$

Since we know $R_{ap}^{(n)}(x,\tau;m)=R_{pa}^{(n)}(x,-\tau;m)$, and thus $S_{ap}^{(n)}(x;f,m)=S_{pa}^{(n)}(x;-f,m)$ is true for both symmetric and non-symmetric cross-correlation and cross-spectral functions, the space–time correlations are transformed into the correct frame of reference for input into the low-dimensional estimate, that is by substituting $S_{ap}^{(n)}(x;f,m)$ in place of $S_{pa}^{(n)}(x;-f,m)$. Because of the simplification in (3.13), the linear system of equations (3.6) reduces to an independent series of equations. This removes the burden of having to invert a matrix which can be highly ill-conditioned under certain circumstances.

Complex spectral estimation coefficients are obtained,

$$b^{(n)}(x;f,m)=\frac{S_{ap}^{(n)}(x;f,m)}{S_{pp}(f,m)}, \tag{3.15}$$

thus completing the link between the velocity and pressure fields in mode-number/frequency space. We here point out that (3.15) comprises the exact form of (6) in Borée (2003), aside from our choice of Fourier-azimuthal decomposition and frequency.

An estimate of the POD expansion coefficient's temporal frequency is performed following (3.5),

$$\grave{a}^{(n)}(x;f,m)=b^{(n)}(x;f,m)p(f,m), \tag{3.16}$$

from which its temporal characteristics are then resolved: $\grave{a}^{(n)}(x;f,m)\rightarrow\grave{a}^{(n)}(x,t;m)$ via inverse Fourier transformation.

To complete the process, an expansion of the time-varying coefficients onto the POD bases is performed,

$$\grave{u}_i^{(k)}(r,x,t;m)=\sum_{n=1}^{k}\grave{a}^{(n)}(x,t;m)\Phi_i^{(n)}(r,x;m), \tag{3.17}$$

followed by a transformation from m to space θ,

$$\grave{u}_i(r,\theta,x,t)=\int_{-\infty}^{\infty}\grave{u}_i(r,x,t;m)\mathrm{e}^{\mathrm{i}m\vartheta}\,\mathrm{d}m. \tag{3.18}$$

As we see on the left-hand side of (3.18), the low-dimensional estimate is fully three-dimensional, comprises all three components of the velocity field and is time resolved. A cartoon illustration of this procedure is shown in figure 4 where the pressure and velocity fields are represented using Fourier-azimuthal modes ($m=5$) and ($m=8$). The selection of these mode numbers is only for the clarity of this illustration since, as will be shown, only the first few Fourier-modes ($m=0$, 1 and 2) will be included in the model estimate. The radial extents of the velocity Fourier-modes are optimized using POD, of which the shapes of the first bases (for both Fourier-modes at $x/D=4$) are illustrated. The objective thus being to determine a transfer function (spectral estimation coefficient) that links the two fields (for each non-orthogonal combination of modes) through their low-order coefficients. We must, however, exert some caution concerning the linear estimate of velocity fluctuations from pressure fluctuations with respect to Poisson's equation.

3.3. *Linear truncation of the conditional estimate*

Poisson's equation, derived from the momentum and mass-conservation equations, is expressed for the instantaneous static pressure of an incompressible fluid with constant density as,

$$\frac{1}{\rho}\nabla^2\tilde{p}=-\frac{\partial\tilde{u}_i}{\partial x_j}\frac{\partial\tilde{u}_j}{\partial x_i}, \tag{3.19}$$

where ∇^2 is the Laplacian operator, and the tilde represents an instantaneous quantity. Following the procedure of George *et al.* (1984) and Townsend (1976), the right- and left-hand sides of (3.19) are decomposed into mean and fluctuating quantities from

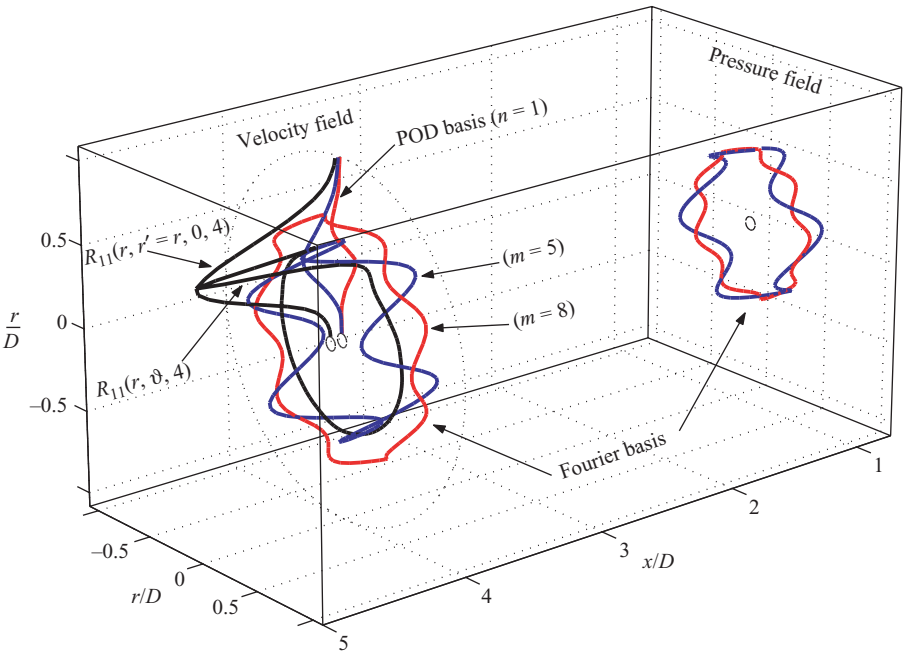

FIGURE 4. Cartoon illustration of the 'Modified Complementary Technique' applied to the Mach 0.85 jet using pressure signatures near the nozzle exit.

which we obtain,

$$\frac{1}{\rho}p(\boldsymbol{y},t) = -\frac{1}{4\pi}\int\left[\frac{\partial U_i}{\partial x_j}\frac{\partial u_j}{\partial x_i}+\frac{\partial U_j}{\partial x_i}\frac{\partial u_i}{\partial x_j}\right]\frac{\mathrm{d}^3\boldsymbol{x}}{|\boldsymbol{x}-\boldsymbol{y}|} - \frac{1}{4\pi}\int\frac{\partial^2}{\partial x_i\partial x_j}\left[u_iu_j-\langle u_iu_j\rangle\right]\frac{\mathrm{d}^3\boldsymbol{x}}{|\boldsymbol{x}-\boldsymbol{y}|}. \tag{3.20}$$

Here (3.20), the pressure field is shown to comprise two energy contributions: (i) interactions of the turbulence with the mean shear (linear, shear-noise), (ii) interactions of the turbulence with the turbulence (quadratic, self-noise). Since the conditional estimate comprises only linear coefficients, the significance of the higher-order terms, those which have been truncated, are discussed here.

Michalke & Fuchs (1975) suggested that in the axisymmetric jet, the shear-noise terms were the dominant sources in certain regions of the flow, and with respect to certain directions of noise radiation. Laufer & Yen (1983) showed that the far-field pressure correlated best with the square of the velocity fluctuations whereas the near-field pressure varied linearly and was attributed to an interaction between the fundamental (frequency) and the first subharmonic, or from the self-interaction of the second harmonic. These same findings have also been reported in a number of other flow scenarios including the subsonic (Mach 0.2 to 0.73) cavity flow studies of Murray & Ukeiley (2006) whereby the quadratic term (u_1u_1) never exceeded 0.20 when correlated with the surface pressure, whereas the linear term (u_1, u_2) achieved correlation levels as high as 0.70 in some instances (while these results were shown for zero time-lag, it is conceivable that at non-zero time lags, the quadratic terms could become dominant). Thus, as it has been shown how the pressure field in the periphery of the hydrodynamic region is driven principally by a linear dependence

with the turbulent large-scale flow instabilities, we do recognize that the inclusion of higher-order coefficients would eventually improve the accuracy of the model estimate. Furthermore, Tinney *et al.* (2007) showed that while a conditional estimate may have comprised only linear estimation coefficients, the estimated velocity field had not been linearized and contained third- and fourth-order terms with spatial dependencies. The fourth order-terms are associated with the self-components of the quadrupole sources of noise (Ribner 1969).

4. Pressure–velocity coupling

Aside from producing a low-dimensional estimate of a subsonic jet flow, the coupling of the pressure field with the velocity field (in a reduced-order domain and a space–time coordinate) presents a unique opportunity to analyse the average relationship between the source field (turbulence) and the reactive components of the pressure field as they are driven by the most compact structures in the flow. These space–time correlations were formed using both scalar and vector forms of the POD, albeit the coefficients from the scalar decomposition are used specifically in this discussion since the pressure field has been shown by Lau *et al.* (1972) to react differently to the axial and radial components of velocity. Such an analysis is more involved with the coefficients from the vector POD owing to a toggling effect between POD modes and components of velocity. The space–time correlations are complex since an azimuthal offset (12.5°) exists between the azimuthal pressure grid and the azimuthal velocity grid, a correction to which is not necessary since the problem is performed using complex functions.

Since the POD bases are incapable of determining phase, the signs of the eigenfunctions are manipulated in order to improve the consistency (in x) of the space–time correlations. This is inconsequential to the low-order reconstruction (it will also improve a subgrid interpolation scheme to be performed later), as is seen in the following sequence of equations using a simplified POD basis from the scalar application of the technique (similarly applied to the vector form), where $\breve{\phi}_i^{(n)}(r) = -\phi_i^{(n)}(r)$,

$$a^{(n)}(t) = \int_R u_i(r,t)\phi_i^{(n)}(r) r \,\mathrm{d}r, \tag{4.1a}$$

$$\breve{a}^{(n)}(t) = \int_R u_i(r,t)\breve{\phi}_i^{(n)}(r) r \,\mathrm{d}r, \tag{4.1b}$$

$$\begin{aligned} u_i(r,t) &= \sum_n^{cN} a^{(n)}(t)\phi_i^{(n)}(r) \\ &= \sum_n^{cN} \breve{a}^{(n)}(t)\breve{\phi}_i^{(n)}(r). \end{aligned} \tag{4.2}$$

The process of selectively changing the sign of the POD bases was performed by first establishing a reference shape ($\gamma_i^{(n)}(r;m)$), obtained from the POD basis at the first axial position in the flow ($x/D = 3$),

$$\gamma_i^{(n)}(r;m) = \phi_i^{(n)}(r,3;m). \tag{4.3}$$

The reference shape was then projected onto the POD basis at each axial station and then integrated over the spatial domain (R). The sign that resulted from the

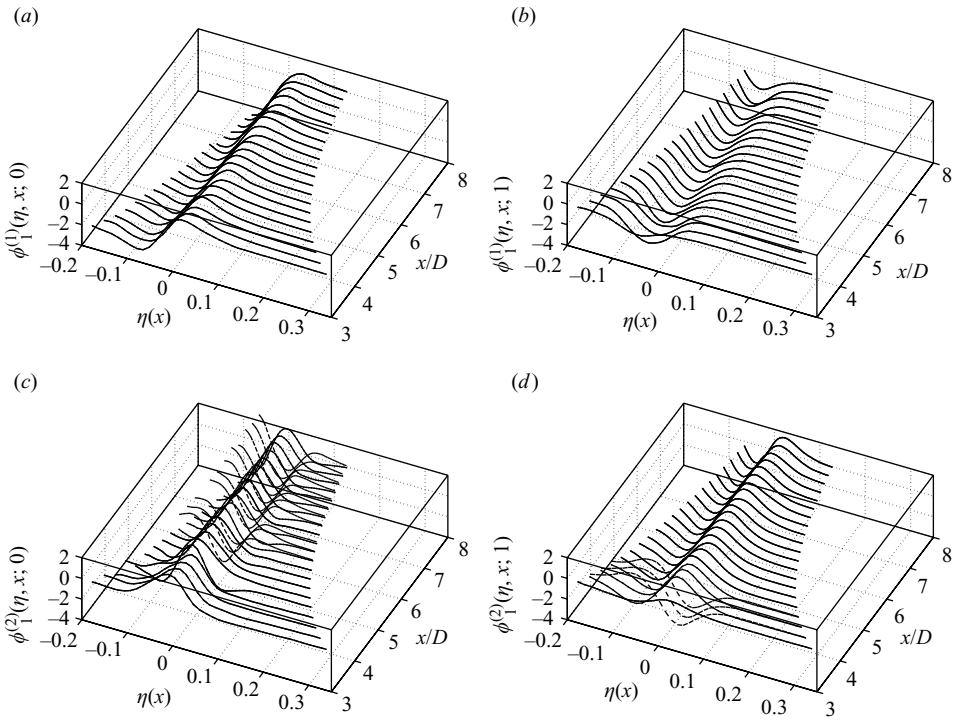

FIGURE 5. Spatial distribution of the POD bases $\phi_i^{(n)}(r, x; m)$ from the scalar decomposition of the axial velocity ($i = 1$) for (*a*) $n = 1, m = 0$, (*b*) $n = 1, m = 1$, (*c*) $n = 2, m = 0$, and (*d*) $n = 2, m = 1$.

integration (positive: in-phase; negative: out-of-phase) determined whether the POD basis was to be flipped. The process was repeated independently for all Fourier ($m = 0 : M/2 + 1$) and POD ($1 : Nc$) modes and for the real and imaginary parts separately. The latter of which was necessary to preserve azimuthal asymmetries in the velocity field. (Azimuthal symmetry was not assumed, though was found to exist within the same order of magnitude as the measurement uncertainty. See figure 12 (*a*, *b*) of Tinney *et al.* (2008).) The POD basis thus comprised a complex function.

A sample set of the corrected (flipped) eigenfunctions is shown in figure 5 using the first two POD and Fourier mode combinations ($n = 1, 2$, $m = 0, 1$) from the scalar decomposition of the axial velocity. The similarity variable $\eta(x)$ has been used and the spatial evolutions of these eigenfunctions are presented. The shape of the original functions has been identified using dashed lines and occurred (for this particular mode combination) for the second POD mode (figure 5 *c*, *d*). In general, the eigenfunctions corresponding to the first few turbulent velocity modes (POD and Fourier) were incapable of collapsing as well as the turbulent statistics. Evidence of this has already been shown in figure 21 (*a*, *b*) of Part 1 using a low-order reconstruction of the kernel. This is expected since the eigenfunctions represent the mean square evolution of the turbulent modes, and thus the evolution of the various components that manifest the full turbulent statistics. To effectively collapse the POD bases, we would have to determine the spatial growth rate of each eigenfunction (appearing still to be linear), which are unique since the near-field region of the turbulent jet comprises a spectrum

of modes that exchange/transfer energy as it undergoes streamwise growth, saturation and decay, unlike the far-field region (Gamard, Jung & George 2004).

The simplicity of selectively changing the sign of the eigenfunctions was based on the spatial similarity of these functions for the axisymmetric jet flow, following the coordinate system that was chosen. After the process was completed for the vector application, the new POD bases ($\breve{\Phi}_i^{(n)}$) were inserted in place of ($\Phi_i^{(n)}$) in (3.7) and (3.17).

4.1. *Space–time correlations*

The space–time correlations from which the pressure–velocity cross-spectra are obtained are illustrated in figure 6 appropriately normalized using the expression,

$$\xi_i^{(n)}(x,\tau;m) = \frac{\left\langle a_i^{(n)}(x,t_s;m)p^*(t-\tau;\beta)\right\rangle \delta_{(m,\beta)}}{\lambda_i^{(n)(1/2)}(x;m)B_{pp}^{(1/2)}(\beta)\delta_{(m,\beta)}}, \tag{4.4}$$

for all three velocity components from the scalar POD decomposition. Subscripts have been included in (4.4) to differentiate between the different velocity components used in the scalar POD while the range of the contour levels is determined by the maximum and minimum values. The correlations have also been limited to only the first POD mode, though the amplitude of the correlation was found to decay rapidly with increasing POD mode number, making it difficult to determine whether any such pattern did exist beyond mode 3. Moving from left to right in this figure corresponds to different Fourier-azimuthal mode numbers which we have also truncated to only the first four azimuthal modes ($m = 0, 1, 2, 3$) since a similar filtering effect is observed with increasing Fourier-mode number. As for the domain of the correlations, those pertaining to the axial and radial components of velocity have been illustrated using the real part of the correlation function, while the azimuthal velocity component comprises the imaginary part. The selection of the complex domain was based upon the amplitude of the correlations, those that were strongest being displayed here.

The decay of the correlation amplitudes with increasing mode numbers (POD and Fourier) are not surprising, and were in fact anticipated, following the discussions of Batchelor (1951), Michalke & Fuchs (1975) and George *et al.* (1984). Though, as we are able to view the spatial and temporal relationship between the low-order modes of the pressure and velocity fields, it is perhaps obvious that the Lagrangian time scale decays faster with increasing mode number, since it is the low-speed regions of the jet flow that manifest the higher-velocity modes (see figure 21*a*, *b* of Part 1) and where the turbulent events become less compact and more dispersive in their life cycle (Yule 1978; Hussain & Clark 1981). Therefore, although we are able to achieve correlation levels of the order of 20 % for the $m = 3$ correlations, their rapid decay in a convective frame is evidence of the short life span of these events and our inability to estimate accurately their behaviour beyond a few jet diameters. With respect to the lowest-order modes, $m = 0$ and 1, they are clearly shown here to manifest survival distances much larger than the jet diameter.

Former attempts to quantify the link between the turbulent events in a jet flow to the pressure field within the periphery of the hydrodynamic region found coherence amplitudes between the raw velocity and raw pressure signals $\langle u_1(r,x,t)p(t-\tau,\theta)\rangle$ of the order of $\sim$25 % (Hall *et al.* 2005). Slightly higher correlations were observed (35–40 %) when the velocity was reduced to its low-order coefficients (scalar decomposition) and linked to the raw pressure field; $\langle a^{(n)}(x,t_s;m)p(t_s-\tau,\theta)\rangle$ (Tinney *et al.* 2005). In the present study, we have reduced both the velocity field (all three components) and the raw pressure signals into their low-order coefficients, from which

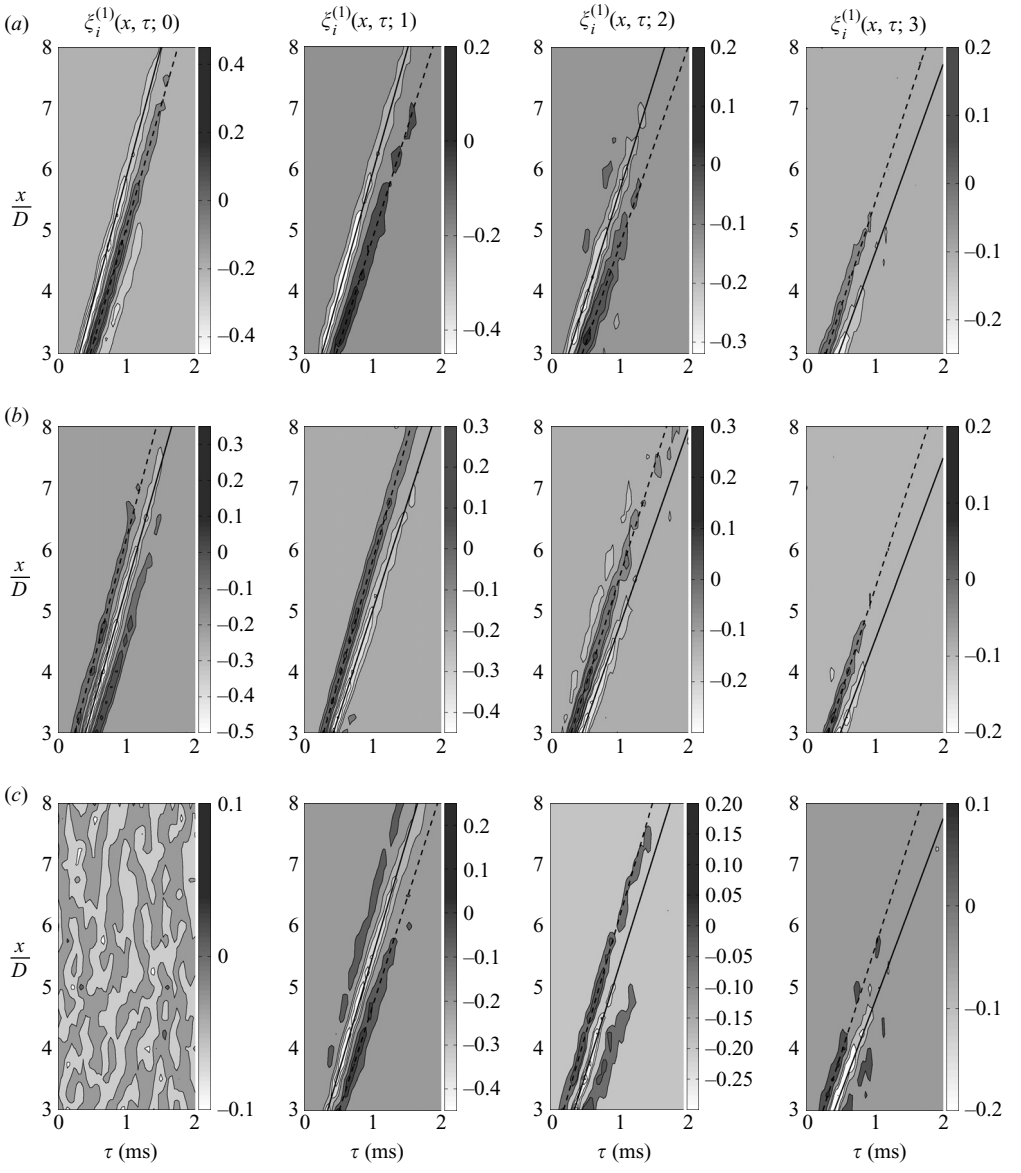

FIGURE 6. Pressure mode and velocity mode (scalar POD) space–time correlations using the first velocity POD mode and Fourier modes 0 to 3 (from left to right) from the (*a*) axial, (*b*) radial and (*c*) azimuthal scalar decompositions of the velocity.

the joint second-order statistics have been created ($\langle a^{(n)}(x,t_s;m)p^*(t_s+\tau;\beta)\rangle\delta_{(m,\beta)}$), and shown to manifest correlations of the order of $\sim$50 %. This is a dramatic improvement over former attempts and the advantages obtained with such a low-order system.

4.2. *Convection speeds*

An effort was made to ascertain the convective behaviour (U_c) of the turbulent source field (now expressed in terms of POD and Fourier-azimuthal modes) as seen by the stationary pressure array. This was performed by best-fitting a line arbitrarily

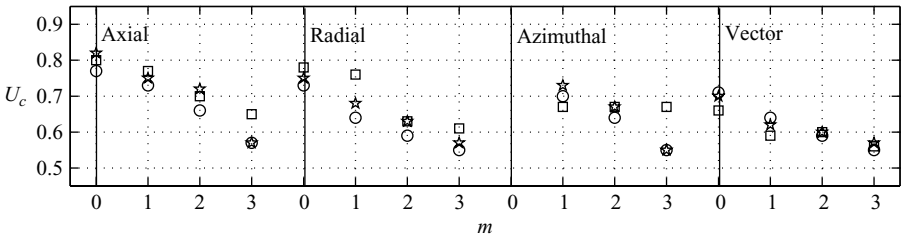

FIGURE 7. Convection velocity of the first (○); second (⋆); and third (□) POD modes for the axial, radial and azimuthal velocity components.

to the first maximum negative (solid) and positive (dashed) correlation peaks in figure 6, of which the slopes from the negative peaks have been summarized in figure 7 using solutions from both the scalar and vector POD. The trends that are produced from this are anticipated following the results of Glauser & George (1987) and Citriniti & George (2000) who showed the frequency dependence of the POD expansion coefficients. Lower Fourier mode numbers show the high-speed high-frequency events while higher mode numbers comprise the low-speed low-frequency events. Typical convection speeds of the order of $\sim 0.60U_j$ have been reported on numerous occasions in both subsonic and supersonic shear flows. A fraction of these investigations (e.g. Ko & Davies 1971; Kerhervé *et al.* 2004) have demonstrated the radial dependence of the jet convection velocity whereby the high-speed side of the shear layer comprises speeds that were lower than the mean velocity, but faster than the mean velocity in the low-speed side of the jet shear layer. To this end, the spatial topology of the POD basis (unlike Fourier) allows us to identify the radial position in the flow where the various flow modes reside. A subset of the POD bases have already been illustrated in figure 5 to demonstrate their spatial topology. By incorporating a full measure of the cross-spectral relationship between these two events (pressure and velocity), the temporal phase lag is embedded in the spectral estimation coefficients and the ability to estimate accurately the space–time characteristics of the various flow modes is improved. Consistency of this space–time behaviour is observed between the solutions using the vector and scalar forms of the POD.

4.3. *Spatial phase dependencies*

The spatial dependencies between the pressure and velocity fields within the hydrodynamic periphery of a jet flow were first demonstrated by Lau *et al.* (1972) using synchronous microphone and cross-wire measurements. They found the axial velocity component to be in antiphase with the fluctuating pressure in the jet's potential core, but in phase in the entrainment region, whereas the radial component of velocity was always in quadrature with the pressure. Thus, the streamwise fluctuations were always 90° out of phase with the radial fluctuations, the streamwise component having been found to lead the radial component in the entrainment region while lagging in the potential core. We should expect the same phenomena (as shown by Lau *et al.* 1972), at least for the most energetic velocity and pressure modes, to be present in the space–time correlations in figure 6.

To illustrate this, the pressure–velocity mode correlations (using (4.4)) have been extracted using the first four Fourier-azimuthal modes (figure 8) and the first POD mode from the vector and scalar decompositions of the velocity at $x/D = 3.0$. Since we are unable to determine the correct sign for the correlations without demonstrating the shape of the POD bases, we will concern ourselves with the temporal phase

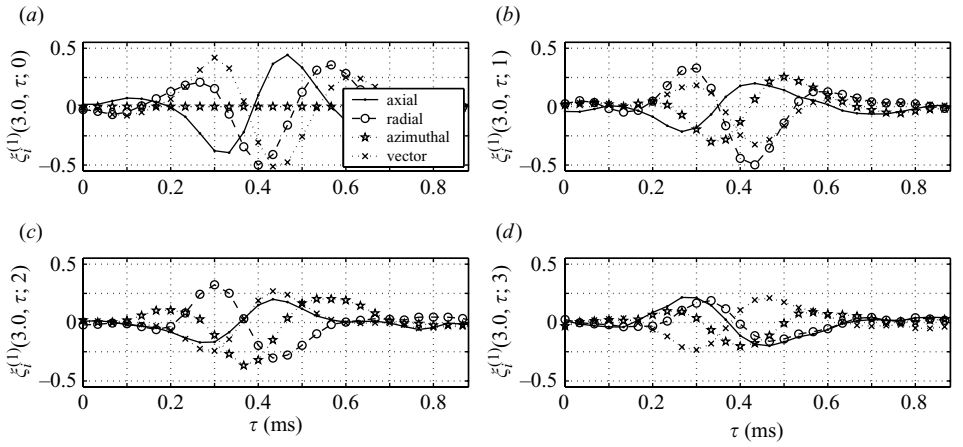

FIGURE 8. Pressure mode and velocity mode (scalar and vector POD) space–time correlations at $x/D = 3.0$ using the first velocity POD mode and Fourier modes (*a*) 0, (*b*) 1, (*c*) 2 and (*d*) 3.

relationship between the correlation peaks. For the column mode structure ($m = 0$ in figure 8*a*), the axial and radial components are shown to be out of phase by exactly 90°, within the resolution of the discretization of the time step. The correlation with the vector component is shown here to be similar in shape and opposite in sign to the axial correlation, thus suggesting that the $n = 1$, $m = 0$ mode from the vector solution manifests most of its energy from the first axial POD and Fourier mode. For the higher Fourier modes, i.e. $m = 1, 2, 3$ in figure 8 (*b–d*), the interpretation becomes more difficult, as we concern ourselves with azimuthal straining of the large-scale vortex structure.

Similarly to figure 8, the pressure velocity mode correlations are shown in figure 9 by overlapping different Fourier modes for a given component of velocity (u, v and w), respectively, and axial station in the flow ($x/D = 3.0$ and 5.5). As we can see, the pressure field responds differently to the excitation from different Fourier modes of the velocity field. Once more, the cross-correlations at $x/D = 3.0$ comprise wavelengths that are shorter when compared to the correlations at $x/D = 5.5$. Thus, there is a sensitivity in the pressure field to the turbulent structure's growth and changing time scale with downstream position in the flow. By incorporating spectral estimation coefficients, the time scales of these turbulent events, as they relate (linearly) to the pressure field, are better preserved.

5. Low-dimensional time-resolved estimate

A low-dimensional time-dependent reconstruction of the velocity field from the pressure field is presented to develop an intuition for the three-dimensional three-component time-resolved low-order behaviour of the jet flow. This is performed by computing the pressure–velocity-mode cross-spectra (3.14) directly from the space–time correlations. A sample cross-spectra is shown in figure 10 for the real and imaginary components, respectively. The envelope comprising the characteristic frequency is shown to shift from events that manifest high frequencies upstream ($St_D \approx 0.45$ at $x/D = 3.0$) to low frequencies downstream ($St_D \approx 0.2$ at $x/D = 8.0$), consistent with the eigenvalue spectra trends illustrated by Ukeiley *et al.* (1999). Thus, as we have seen in the space–time correlations, the changing time scales of the

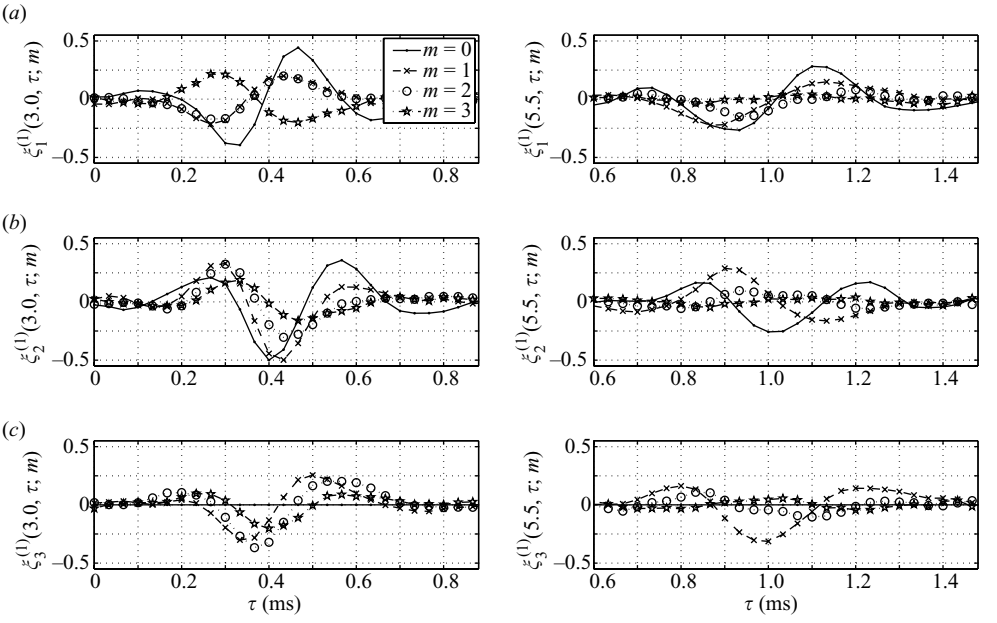

FIGURE 9. Pressure mode and velocity mode (scalar POD) space–time correlations using the first three velocity POD modes (from top to bottom) and Fourier modes 0 through 3 from the (*a*) axial, (*b*) radial and (*c*) azimuthal scalar decompositions of the velocity at $x/D = 3.0$ and 5.0.

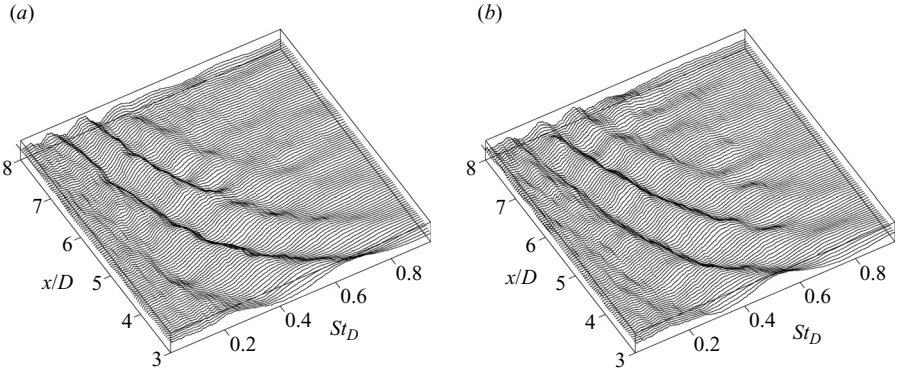

FIGURE 10. Pressure–velocity-mode cross-spectra from $n = 1, m = 1$ of the radial component of velocity for the complex (*a*) real and (*b*) imaginary domains.

most energetic flow modes are preserved in the spectral estimate and are seen here in the pressure–velocity-mode cross-spectra.

While the bulk of the space–time correlations have been presented using the POD bases from the scalar decomposition, the low-dimensional estimate is constructed using the POD bases from the vector decomposition. The vector POD has the added benefit of ensuring a basis set which preserves orthogonality between both the POD modes and the different components of the velocity field, as this is the most optimal way of reconstructing the low-dimensional topology of the flow. Also, the integration of the Reynolds shear-stress terms in the vector POD is important as they are responsible for various flow-related phenomena including transport, vortex

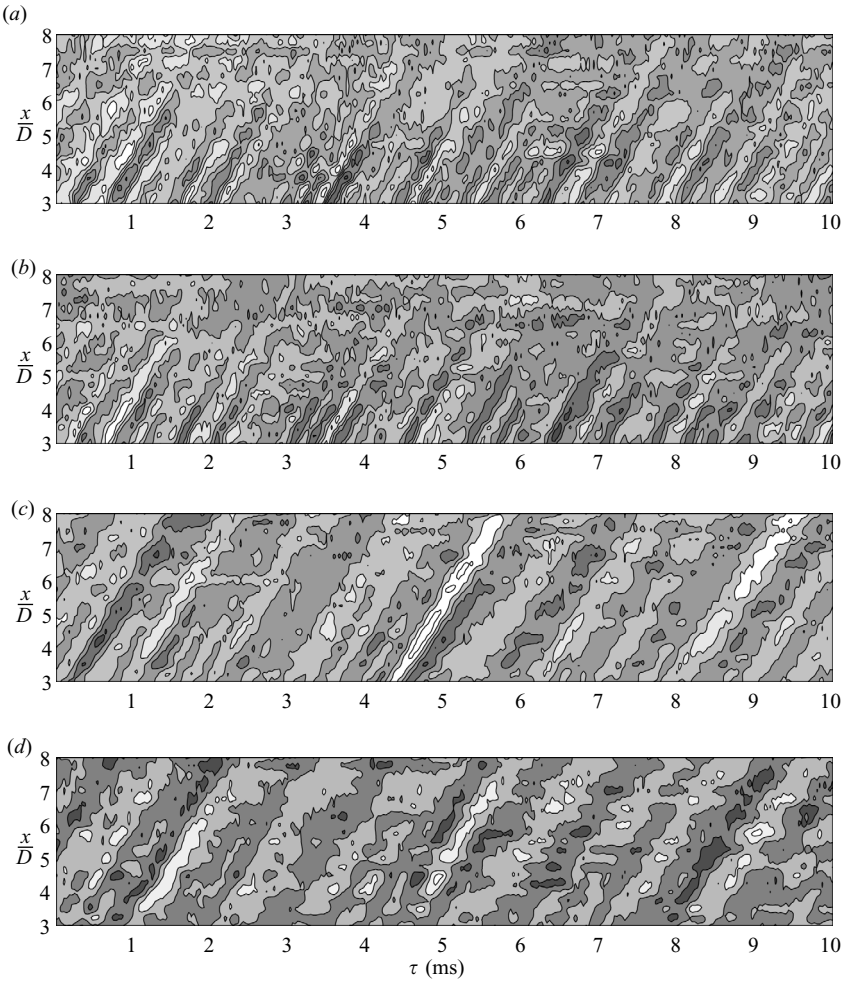

FIGURE 11. Space–time contour of the random POD expansion coefficients (vector decomposition) from the spectral estimate. (*a*) $n=1$, $m=0$, (*b*) $n=2$, $m=0$, (*c*) $n=1$, $m=1$, (*d*) $n=2$, $m=1$. Light and dark contours corresponding to positive and negative fluctuations, respectively.

stretching and turbulence production. A subset of the pressure–velocity-mode space–time correlations were demonstrated in figure 8, along with an estimate of their convection speeds in figure 7, and were found to share many similar features with the correlations generated using the POD bases from the scalar form.

Sample space–time topologies of the estimated POD expansion coefficients are shown in figure 11 using the first two POD and Fourier modes from the vector decomposition. Clear trends can be seen in all of the contours thus characterizing the convective nature of the low-order turbulent modes relative to the stationary pressure array. Similar topological characteristics where found in the higher POD mode combinations, the trends, however, becoming more difficult to decipher beyond POD mode 3 and the fourth Fourier mode ($m=3$) following the discussion in § 4.1. In figure 11 (*a*, *b*), the trend for the first two POD modes of the column mode structure decay around $x/D=6.0$, after which it becomes difficult to separate the convecting

structures from uncertainties in the estimate. In contrast to the column mode, the first two POD modes of the helical mode (figure 11 *c*, *d*) remain fairly consistent until the end of the measurement region ($x/D = 8.0$). Similar effects were found in the estimate of Tinney *et al.* (2007) whereby the helical mode became the dominant turbulent mode after the collapse of the potential core as observed by the pressure field. While these results are not necessarily striking considering the results of Iqbal & Thomas (2007) and Part 1, what is striking is the sensitivity of the pressure field to the events which are up to 7 jet diameters away at $x/D = 8.0$ from the pressure array situated at $x/D = 0.875$.

5.1. *Sub-grid interpolation*

While the raw PIV measurement plane comprised spatial resolutions of the order of $\Delta y/D = 5.0 \times 10^{-2}$ and $\Delta z/D = 3.3 \times 10^{-2}$ (see Part 1), the axial grid density was larger at $x/D = 0.25$. In an effort to reduce this discrepancy, a subgrid interpolation of the axial dimension was performed using a two-dimensional spline as described by Tinney *et al.* (2007). This was performed to both the POD bases ($\check{\Phi}_i^{(n)}$ from § 4) and the real and imaginary domains of the complex cross-spectra (3.14). A sample of the interpolated cross-spectra is shown in figure 10 and was found to have little effect on the quality of the estimate. The final grid density in the axial direction was $x/D = 6.25 \times 10^{-2}$ and was necessary so that the full velocity gradient tensor ($\nabla \boldsymbol{u}$) could be calculated in a subsequent part of this discussion.

5.2. *A slice of the jet*

The first experimental low-dimensional time-dependent reconstruction of the axisymmetric jet was performed by Citriniti & George (2000) who showed evidence of both ring vortices and streamwise rib vortices in the shear layer. An azimuthally coherent 'volcano-like' eruption was found to occur and was thought to be the result of a 'leap-frogging' of the azimuthally coherent ring vortex as had been proposed by Grinstein, Glauser & George (1995). The 'volcano' eruption forced a highly coherent mass of fluid through the centre of the jet while entraining higher modal events into the potential core after its passing. Several life-cycle reconstructions were performed by Citriniti & George (2000) to show how the entrainment of the highly azimuthally coherent events (mode 6) had occurred between successive eruptions and represented the topology of the jet slice during the bulk of the time steps. Therefore, although the 'volcano-like' eruption was very rapid in its life-cycle, it occurred for only a small fraction of the time, but with an activity that comprised most of the turbulent energy. The eruption was also found to occur with a regularity that matched well with the jet's peak Strouhal number. Since this seminal work (Citriniti & George 2000), several attempts have been made to uncover the dynamics of this characteristic event under a range of Reynolds numbers and Mach numbers (Taylor, Ukeiley & Glauser 2001; Jung, Gamard & George 2004; Iqbal & Thomas 2007).

The relevance of the higher-Mach-number studies is based on a well-known understanding that the dominant region for jet-noise radiation occurs just after the collapse of the potential core. The identification of this event near the collapse of the potential core in the low-Reynolds-number low-Mach-number studies suggests that this 'volcano-like' eruption may be the prominent sound-source event in the axisymmetric shear layer. A concerted undertaking by Ukeiley *et al.* (1999) and Taylor *et al.* (2001) showed that the POD eigenspectra in the Mach 0.30 and 0.60 jet flow shared nearly identical features with the low-speed jet measurements of Glauser & George (1987) and Citriniti & George (2000). The work of Ukeiley *et al.* (1999) was extended to the Mach 0.85 flow; however, owing to high probe breakage,

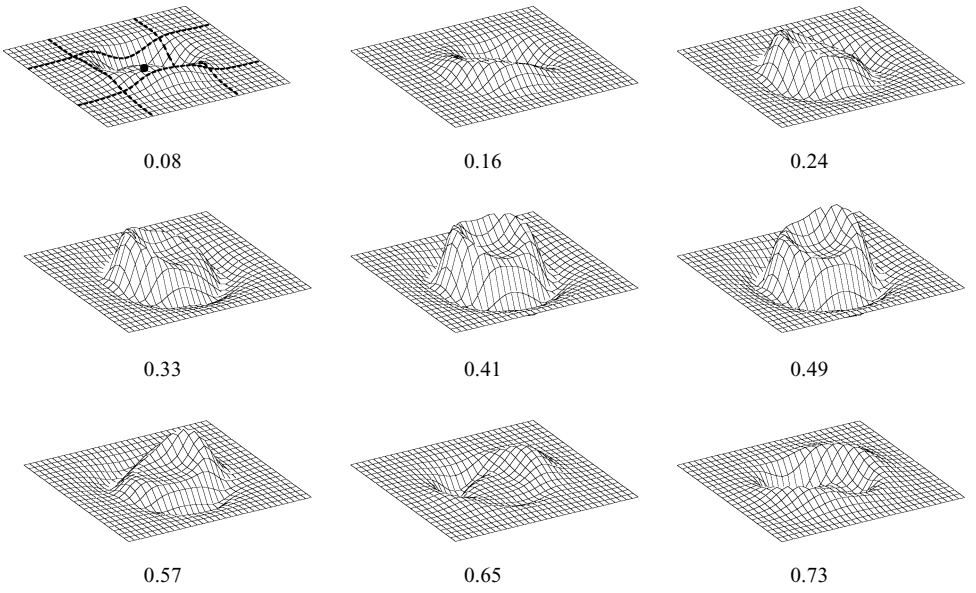

FIGURE 12. Time series reconstruction of the axial component of velocity at $x/D = 3.0$ during a period of 'volcano-like' eruption.

the modal analysis could not be performed. Mass-flux spectra at several points in the flow from the Mach 0.85 jet measurements were compared with those from the Mach 0.30 and 0.60 jet studies to show that the low-order dynamical behaviour of the axisymmetric jet was relatively independent of Mach number and Reynolds number studied (beyond a certain Reynolds number following the discussion of Glauser & George 1987). Hileman *et al.* (2005) showed that immediately before the periods of jet-noise emission, the cross-stream and streamwise planes of the jet (triggered images of illuminated condensed water particles in a cold jet that were conditionally sampled by an array of far-field microphones) demonstrated positive intensity fluctuations at the jet centreline in a region immediately past the end of the potential core. One convective time scale before noise emission, a series of robust flow features were observed, the flow features being consistent with the entrainment of ambient fluid due to large-scale motion, and what we here consider to be the early stages of 'volcano-like' bursting, as was described by Citriniti & George (2000). Thus it is fairly certain that the 'volcano-like' eruption that has been found in the incompressible lower-Reynolds-number flows would exist in the higher Mach numbers and that this event is probably associated with the sources of jet noise in the vicinity of the end of the potential core. An attempt to uncover this 'volcano-like' eruption is made in the current discussion using the low-dimensional estimate of the Mach 0.85 jet and is, in fact, one of the underlying motivations of this work.

The axial component of velocity is purposely selected from the low-dimensional estimate in the current study in order to compare it with the time-dependent models of others (Citriniti & George 2000; Taylor *et al.* 2001; Jung *et al.* 2004; Iqbal & Thomas 2007). Since the low-dimensional estimate is now time dependent ($\Delta t = 1/30\,\mathrm{kHz}$ based on the sampling speed of the pressure array) with respect to the characteristic frequency of the jet flow (estimated to be around $St_D = 0.45$ at $x/D = 3.0$ based on LDA measurements) we are capable of illustrating the life-cycle of this event at Mach 0.85. In figures 12 and 13, a slice across the radial and azimuthal plane

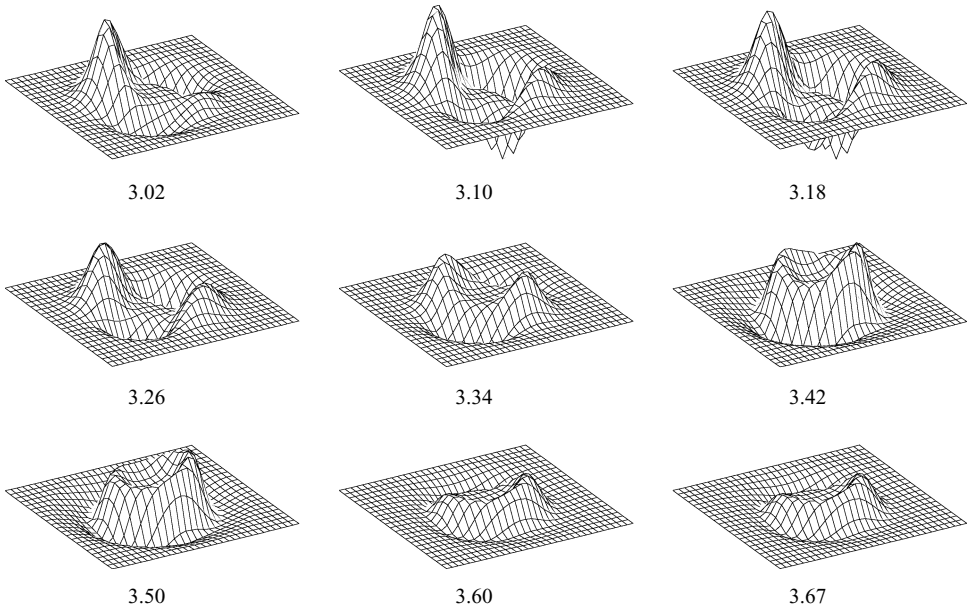

FIGURE 13. As figure 12, but for greater time steps.

at $x/D = 3.0$ is shown for a series of successive time steps, referenced to the same initial time step. The time step shown at the bottom of each snap-shot is defined as $St_D U_j D^{-1} t^{-1}$, using the peak Strouhal number for this location. The two sequences have been purposely selected as they both clearly illustrate the life-cycle of a bursting-like event. Several points are drawn on the first reconstruction in figure 12 (0.08) identifying the centre of the jet at $y/D, z/D = 0$ (closed circle) and the nozzle lip lines at $y/D, z/D = \pm 0.5$ (dashed lines). Since a pressure filtering effect is inherent in the estimate, the reconstructions include only the first few Fourier-azimuthal and POD modes ($m = 0 + 1 + 2$ and $n = 1 + 2$). Although it may be advantageous for us to include the higher-velocity modes in order to fully capture the life-cycle of the 'volcano-like' event, their accuracy is uncertain considering the decay of the correlation function with increasing mode number. Nevertheless, Citriniti & George (2000) have shown how the column mode instability contains the bulk portion of the energy and is captured well in this low-dimensional estimate of the Mach 0.85 jet.

An estimate of 200 time steps was found to produce 15 bursts similar to those shown in figures 12 and 13, resulting in a burst frequency of $St_D \approx 0.41$. It is likely that these bursts are related to the 'volcano-like' eruptions that were observed in the low-Mach-number and Reynolds-number studies of Citriniti & George (2000). However, as the potential core for this jet does not collapse until after 6 jet diameters, these bursting events are most probably an infant form of the 'volcano-like' events. It is impressive to see from these time-series illustrations the persistence of an event that erupts with regularity, occurring similarly at both high and low Reynolds numbers and Mach numbers.

A crude attempt to track the burst events is undertaken. The first burst-like event illustrated in figure 12 is now shown in figure 14 with new axial positions at $x/D = 5.0$ and 7.0, respectively. A time-lag has been inserted using a convection speed, determined from figure 7, of $0.70U_j$. At $x/D = 5.0$, the event comprises similar energy as it did at $x/D = 3.0$. Two jet diameters away ($x/D = 7.0$), the energy of the eruption

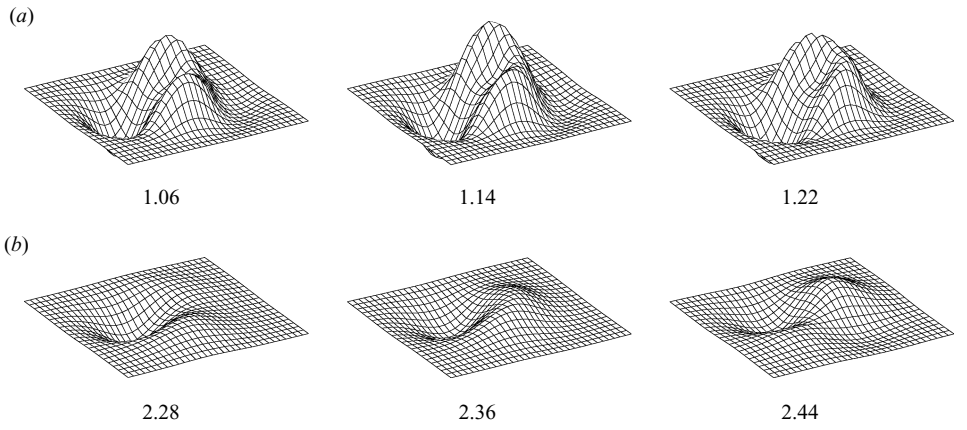

FIGURE 14. Time series reconstruction of the axial velocity component at (*a*) $x/D = 5.0$ and (*b*) $x/D = 7.0$.

has rapidly decayed. These events now cover a larger surface in the (r, θ)-plane; the benefit of having estimated the time-varying POD coefficients which govern the temporal phase of the spatially dependent and empirically derived POD basis set. Also, the shape of the structure at both axial positions shown in figure 14 resembles the helical mode ($m = 1$) event which is complementary to the space–time topologies shown in figure 11. A similar effect was shown by Jung *et al.* (2004) whereby the flow topology immediately after the 'volcano-like' eruption was very weak (a manifestation of lower Fourier modes) followed by disorganized motions that proceeded into the intermediate and far-field regions of the jet. Iso-contours of the vorticity field were shown by Iqbal & Thomas (2007) to have strong helical mode shapes which continued on through the intermediate regions of the jet.

5.3. *Vorticity and the hydrodynamic source field*

A number of schemes have been proposed for identifying vortex cores based on the identification of a local pressure minima. Of particular interest are the well known Q and λ_2 criteria of Hunt, Wray & Moin (1988) and Jeong & Hussain (1995), respectively. Both schemes are Galilean-invariants of the velocity gradient tensor ($\boldsymbol{\nabla u}$) and are derived from the incompressible form ($\boldsymbol{\nabla \cdot} u = 0$) of the Navier–Stokes flow equation. The advantages to either criteria for this application are not clear, considering the uniqueness of the estimated approach developed. For example, as the λ_2 criterion accounts for the excess of rotation rate over the strain rate magnitude on a specified plane (u–v, u–w or v–w), the Q criterion measures the balance in all directions. Thus, we are interested in identifying vortex cores that are a consequence of three-dimensional effects, rather than the satisfaction of two-dimensional criteria (Jeong & Hussain 1995; Chakraborty, Balachandar & Adrian 2005). It has also been argued that the Q criterion, that is, $Q > 0$, does not necessarily imply that the pressure minimum occurs within the region and that there is no explicit connection between a region of positive Q and a region of pressure minimum. Such an effect is worrisome since the low-dimensional estimate is created from the unsteady pressure field in the hydrodynamic periphery of the jet flow. The λ_2 criterion removes this inconsistency of the Q invariant by discarding the effects due to unsteady straining (capable of producing a pressure minimum without vortical motion) and viscous effects (capable of eliminating the pressure minimum in a flow where vortical motion is present).

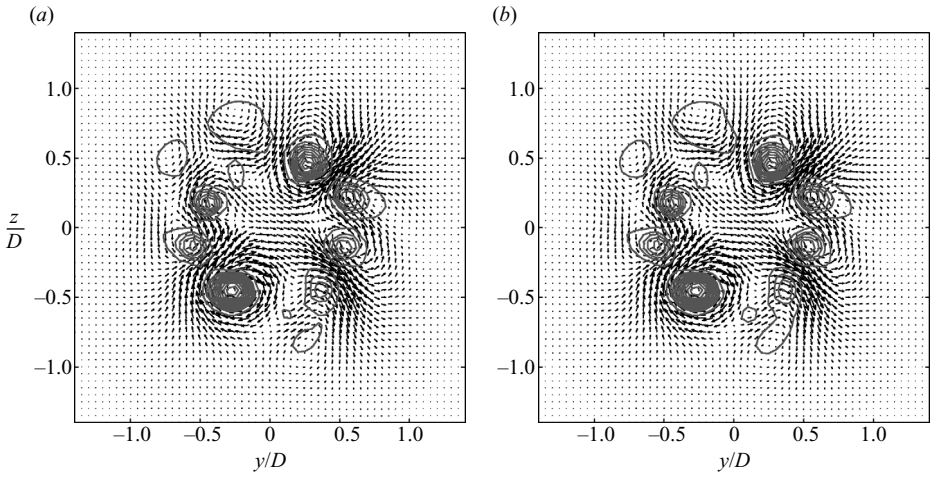

FIGURE 15. Snap-shot of the normal component velocities (vectors) at $x/D = 5.0$ with contours of (*a*) $-\lambda_2$ and (*b*) positive Q.

We will thus derive the solutions to both the λ_2 and Q invariants so as to perform an *ad hoc* comparison between the two schemes for the purposes of visualizing the estimated flow.

The second invariant, Q comprises the symmetric ($\boldsymbol{S}$) and skew-symmetric ($\boldsymbol{\Omega}$) components of the velocity gradient tensor, defined as,

$$Q = \tfrac{1}{2}(\|\boldsymbol{\Omega}\|^2 - \|\boldsymbol{S}\|^2) \tag{5.1}$$

where $\|\boldsymbol{\Omega}\| = \mathrm{tr}[\boldsymbol{\Omega}\boldsymbol{\Omega}^t]^{1/2}$ and $\|\boldsymbol{S}\| = \mathrm{tr}[\boldsymbol{S}\boldsymbol{S}^t]^{1/2}$. A further requirement for Q is that the pressure in the vortex region is expected to be lower than that of the ambient. However, as the low-dimensional estimate of the Mach 0.85 jet flow is based on the hydrodynamic signatures of the pressure field, and its relationship with the turbulent velocity field within the periphery of the hydrodynamic field, there can be no argument as to the sources of the pressure disturbances. That is, disturbances in the ambient field are negligible with respect to the disturbances in the jet. The relationship between the Q and λ_2 criterion can also be shown following the discussion of Jeong & Hussain (1995),

$$Q = -\tfrac{1}{2}\mathrm{tr}(\boldsymbol{S}^2 + \boldsymbol{\Omega}^2) = -\tfrac{1}{2}\mathrm{tr}(\lambda_1 + \lambda_2 + \lambda_3) \tag{5.2}$$

whereby $\lambda_1 \geqslant \lambda_2 \geqslant \lambda_3$ are the eigenvalues of $\boldsymbol{S}^2 + \boldsymbol{\Omega}^2$ and $-\lambda_2$ implies the existence of a pressure minimum and the location of a vortex core along a surface. Thus, where the λ_2 and Q criteria are concerned, the location of a vortex core is identified, respectively, by two negative eigenvalues and by positive Q.

An *ad hoc* comparison between the λ_2 and Q criterion is shown in figure 15 using a low-dimensional reconstruction ($n = 1$ to 3, and $m = 0$ to 6) of the normal component velocities (on a surface) from the original PIV cross-plane measurements at $x/D = 5.0$. The snap-shot illustrates the existence of several counter-rotating vortices centred along the nozzle's lip-line at $r/D = 0.5$; only subtle differences are found between the two schemes. To further challenge these schemes, the vortex methods were compared (not shown) using the low-dimensional estimate comprising the full velocity gradient tensor. To this end, the λ criterion was found to be more sensitive to errors associated with the numerical derivatives and so the Q criterion is employed in the remainder

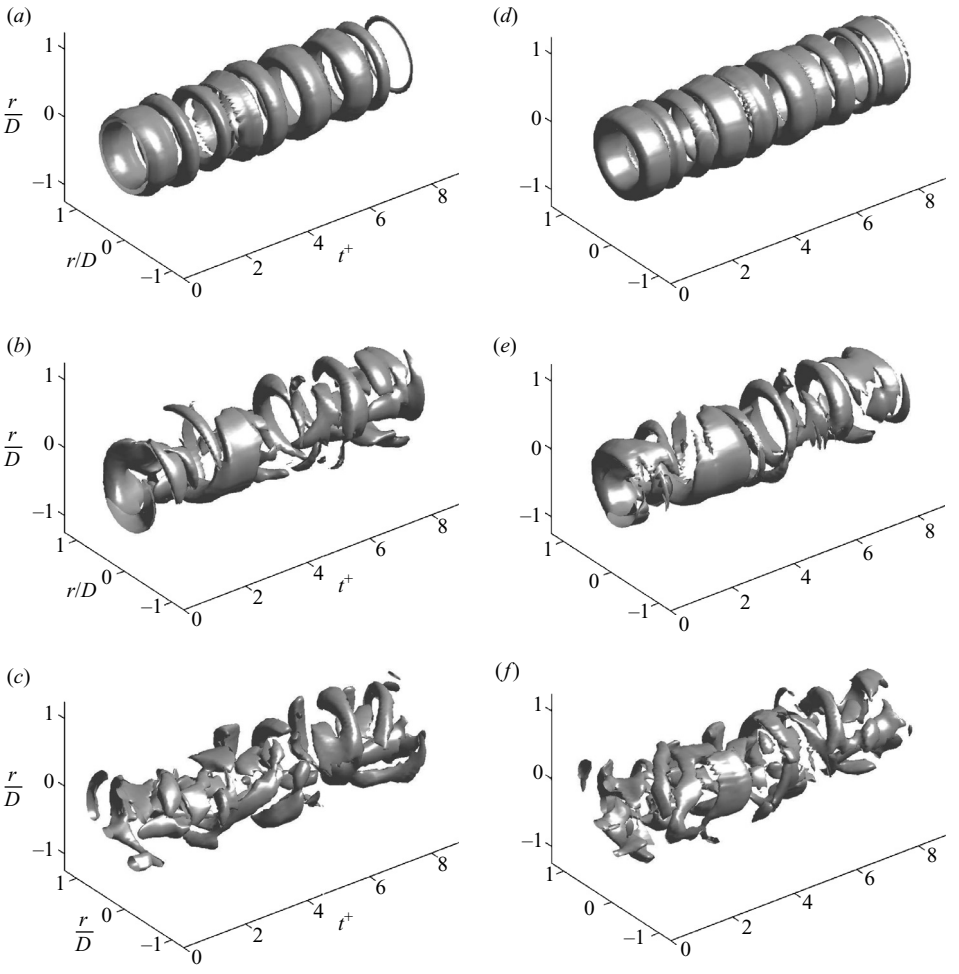

FIGURE 16. Q surfaces of the low-dimensional model at $x/D = 3.0$ using $n = 1$ and (*a*) $m = 0$, (*b*) $m = 0 + 1$ and (*c*) $m = 0 + 1 + 2$. Q surfaces now using $n = 1 + 2$ and (*d*) $m = 0$, (*e*) $m = 0 + 1$ and (*f*) $m = 0 + 1 + 2$ of the same instant in time.

of the discussion, though overall, neither technique appeared significantly superior to the other.

In figure 16, the Q invariant of the full velocity gradient tensor is illustrated at $x/D = 3.0$ using various POD and Fourier-azimuthal mode combinations. The iso-surfaces are generated using 3 % of the maximum iso-surface, as was done by Iqbal & Thomas (2007). The time axis is non-dimensionalized using $t^+ = tU_jD^{-1}$ and the estimate covers a total of 50 time steps. Figures 16(*a*)–16(*c*) have been reconstructed using the first POD mode ($n = 1$) and Fourier-azimuthal modes $m = 0$, $m = 0 + 1$ and $m = 0 + 1 + 2$, respectively. Likewise, the first two POD modes ($n = 1 + 2$) have been used in figure 16(*d*)–16(*f*) with identical Fourier-azimuthal mode combinations, respectively. Thus, figure 16 (*f*) is the most complete representation of the turbulent events at $x/D = 3.0$ which are responsible (linearly) for driving the pressure signatures in the periphery of the hydrodynamic field.

Similar work was undertaken by Iqbal & Thomas (2007) in the Mach 0.30 jet flow using the λ_2 criterion and low-order reconstructions of the radial and azimuthal

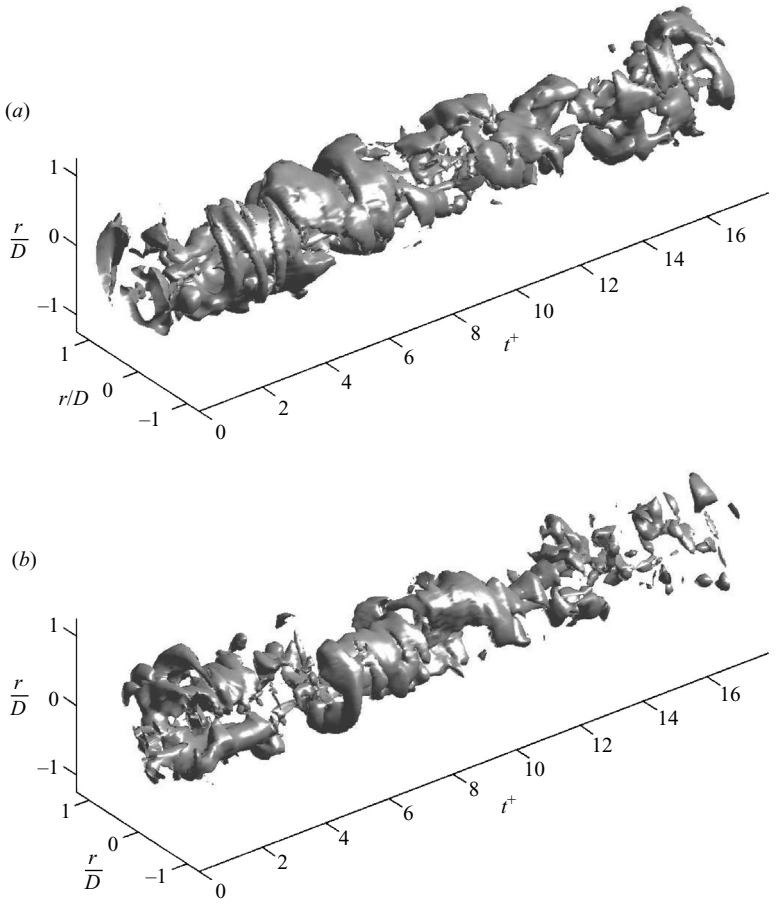

FIGURE 17. Q surfaces of the low-dimensional model using $n = 1 + 2$ and $m = 0 + 1 + 2$ at (*a*) $x/D = 5.0$ and (*b*) $x/D = 7.0$.

vorticity field at several independent axial stations in the flow ($x/D = 3, 4$ and 6). Since Iqbal & Thomas (2007) were not restricted by pressure filtering effects, they were capable of estimating the physical interaction between the $m = 0$ and $m = 5$ azimuthal modes. In particular, they found streamwise vortical braids that appeared to connect the primary shear-layer vortices before the collapse of the potential core with dominant helical mode structures after the collapse of the potential core that continued further downstream into the intermediate region of the jet.

In figure 16 (*a*, *d*), the jet column mode structure manifests regularity in its life-cycle, as was demonstrated earlier. By including the helical mode in the low-dimensional estimate (figure 16 *b*, *e*) the subtle spiralling nature of the jet is shown and the vortex tubes are more compact. In figure 16 (*c*, *f*), the vortex tubes are even more compact in time, although azimuthally coherent events are still evident. In particular, three nearly distinct vortex tubes are shown spiralling in a counterclockwise manner relative to the positive t^+-axis. The behaviour of these events is similar to the radial vorticity reconstructions of Iqbal & Thomas (2007) using the $m = 0 + 1$ at $x/D = 3.0$.

Moving further downstream to $x/D = 5.0$ in figure 17 (*a*), the vorticity field manifests increasingly disorganized events, albeit evidence of azimuthally coherent structures are still present. In particular, azimuthal coherent rings are found at $t^+ \approx 2$ and 6, though

many obscurities exist in between. By $x/D = 7.0$ in figure 17(*b*), the vortex field has become completely disorganized and is most probably due to the low correlation levels at this position that are used in the spectral stochastic estimation. The poor estimation is supported by the fact that the POD results show the dominance of lower azimuthal mode numbers in this region of the flow, which is opposite to what is shown here.

6. Predicting the far-field sound pressure

A prediction of the far-field sound pressure is performed using the low-dimensional estimate of the velocity field comprising a combination of the first two POD modes ($n = 1, 2$) and azimuthal modes $m = 0, 1, 2$. The prediction is performed by solving Lighthill's (1952) equation and thus constitutes an estimate using only those modes whose signatures are energetic enough to drive the events registered in the near-field pressure. Lighthill's theory comprises an explicit solution for the far-field signatures received by an observer submersed in a uniform stagnant fluid with sources of noise being produced by a confined region of intense rotational motion. The analytical solution to Lighthill's equation for an unbounded flow produces an expression which is well known,

$$p'(\boldsymbol{x}, t) = \int_V \frac{\partial^2 T_{ij}}{\partial x_i \partial x_j}\left(\boldsymbol{y}, t - \frac{\boldsymbol{x} - \boldsymbol{y}}{a_\infty}\right)\frac{\mathrm{d}\boldsymbol{y}}{4\pi|\boldsymbol{x} - \boldsymbol{y}|}, \tag{6.1}$$

where a_∞ is the sound speed of the ambient fluid, $\boldsymbol{x}$ and $\boldsymbol{y}$ are the source and observer locations, respectively, and T_{ij} is Lighthill's stress tensor,

$$T_{ij} = \rho \grave{u}_i \grave{u}_j + (p - \rho a_\infty^2)\delta_{ij} - \tau_{ij}. \tag{6.2}$$

Since jet noise is primarily an inviscid process (Crighton 1975), and for mildly heated jets, $(p - \rho a_\infty^2)$ is negligible (Powell 1998), the only contributing term left in (6.2) is the Reynolds stress term: $T_{ij} = \rho \grave{u}_i \grave{u}_j$. Thus, the source field of the low-dimensional estimate is created using a tensor comprising all three components of the velocity field and the density fluctuations associated with the hydrodynamic field are neglected since they are unavailable from the experiment. The definition for the source field is as follows,

$$S = \frac{\partial^2 \grave{u}_i \grave{u}_j}{\partial x_i \partial x_j}, \tag{6.3}$$

and is computed using a second-order-accurate compact finite-difference routine. A higher-order finite-difference scheme (sixth order accurate) was found to have a negligible impact on the quality of the source field and its far-field prediction, since the estimate comprises only the low-order modes of the flow and is therefore not so easily spoiled by small-scale fluctuations. In figure 18, a static illustration of the estimated velocity field using the Q criterion at $x/D = 3.0$ is shown alongside its corresponding source field. Like the vorticity field, the source field is illustrated using isosurfaces at 3 % of the maximum, while positive and negative fluctuations are denoted by grey-scale and blue, respectively.

The locations for the far-field observers were based upon microphone measurements acquired along an arc array at $r/D = 75$ (see Part 1, § 2.8 for a description of these measurements). These measurements were synchronized with the near-field pressure array. Figure 19 shows a prediction of the far-field sound pressures at 90°, 60° and 30° to demonstrate the global topology of the source field as seen by an observer

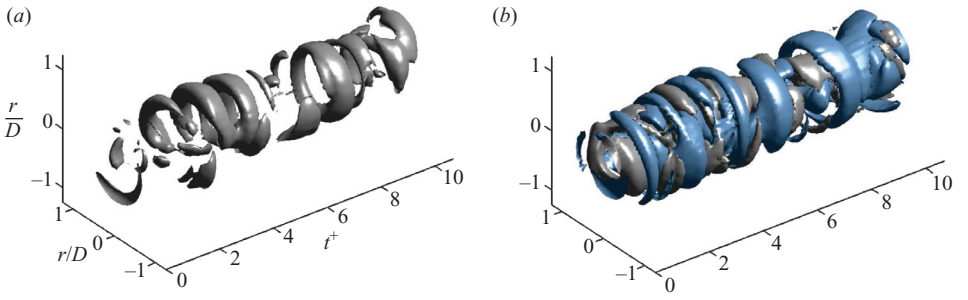

FIGURE 18. (*a*) Q surface of the vorticity field at $x/D = 3.0$ using $n = 1 + 2$ and $m = 0 + 1$ and (*b*) its corresponding source field.

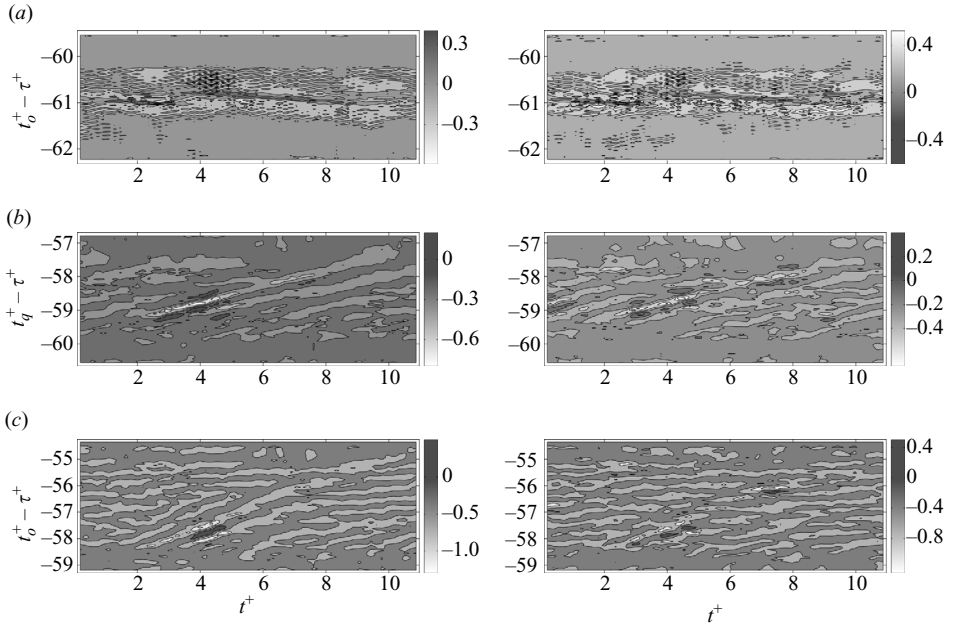

FIGURE 19. Retarded time topologies of the far field pressure ($r/D = 75$) at (*a*) 90°, (*b*) 60° and (*c*) 30° relative to the jet axis using $n = 1$ and $m = 0 + 1$ (left-hand column) and $n = 1 + 2$ and $m = 0 + 1 + 2$ (right-hand column).

in the far field. Ordinate axes have been labelled using the retarded time delay which corresponds to the estimate's initial time step (t_o^+) where $t^+ = 0$. The low-dimensional estimate, from which the acoustic source field is computed, includes a statistically accurate combination of POD and Fourier-azimuthal modes $n = 1$, $m = 0 + 1$ (left-hand column), alongside a quasi-statistically-accurate combination of POD and Fourier-azimuthal modes $n = 1 + 2$, $m = 0 + 1 + 2$ (right-hand column). We have chosen to differentiate the two estimated flow fields in this manner since the first combination of modes ($n = 1$, $m = 0 + 1$) appears from figures 6, 11 to possess a combination of low-order events whose effective lifespan occupies most of the streamwise domain between $x/D = 3.0$ and 8.0. Contrarily, the latter possesses an additional contribution from higher modes ($n = 2$, $m = 2$), the life-span's of which are only accurately estimated over a smaller streamwise domain, after which, their

contribution to the estimate is intermittent between quasi-accurate events and non-physical obscurities, as was illustrated in figure 17.

At 90° (figure 19*a*), the retarded time topologies from both low-dimensional estimates are shown to manifest much higher-frequency motions relative to the signatures observed at 60° and 30° (figures 19*b* and 19*c*, respectively). The topologies at 60° and 30°, demonstrate a convecting pattern of several wave-packet-like source events. Although there is no clear consensus as to the sources of noise in jets, it is nonetheless understood that the high-frequency sound waves observed at sideline and steep angles to the jet axis result from high-frequency motions near the nozzle lip and within the near-field region leading up to the potential core's end. The life-span of these events extend over a shorter streamwise region when compared to the low-frequency flow events in the downstream regions of the flow where the life-span of the structures occupy a much lengthier stretch along the jet axis and therefore produce low-frequency acoustic waves at shallow angles. Likewise, instability waves at high Strouhal numbers amplify more rapidly than instability waves at low Strouhal numbers; low wavenumbers peaking close to the end of the potential core (see Mankbadi & Liu 1984; Viswanathan 2004). Only the low-order features of the turbulence structure have been preserved in this estimate of a Mach 0.85 jet, those which grow proportionately with respect to the expanding shear layer and with time scales that range from high frequencies upstream to low frequencies downstream. In the retarded time topologies of figure 19, the high- and low-frequency signatures observed at 90° and 30°, respectively, are clearly preserved with these low-dimensional techniques. Furthermore, it is clear that different mode number combinations produce distinctly different topologies, ultimately leading to different far-field signatures as a result of net-amplification, net-cancellation, mode-pairing and mode-switching type phenomena.

Power spectral densities and overall sound pressure level (OASPL) directivities from the far-field predictions are compared to the direct measurements obtained from an arc array of microphones (see Part 1). Three different Fourier mode combinations are chosen: $m = 0$, $m = 0 + 1$ and $m = 0 + 1 + 2$, using the first two POD modes. A total of 1200 time steps are computed for each of the three low-dimensional estimates (three different azimuthal mode combinations) corresponding to approximately 50 statistically independent large-scale events (based on D, $f_s = 30\,\mathrm{kHz}$ and a peak Strouhal number of ~ 0.45). The transient time required for the first emitted wave to propagate to the far-field observer has been removed from the time series from which the spectra are computed. The comparison of the power spectral densities are shown in figure 20(*a*) for the 60° observer. An ensemble-averaged spectrum, using a full set of the original far-field microphone data (375 blocks of 2^{13} samples per block acquired at 75 kHz; $\delta f = 9.16$ Hz) is shown juxtaposed with an ensemble-averaged spectrum produced using a reduced set of microphone data comprising 1200 time steps (17 overlapping blocks of 2^7 samples per block resampled to 30 kHz; $\delta f = 234$ Hz). The overlap between the full (2^{13}) and reduced (2^7) sets of data illustrates the quality of the reduced set and is important since the low-dimensional far-field prediction is confined to only 1200 time steps. The power spectral densities have been smoothed using a 10 % bandwidth moving filter. For all POD and Fourier-azimuthal mode combinations considered, an under-prediction in energy is manifest; albeit it is anticipated considering the low-dimensional nature of the estimated flow structures (see Freund & Colonius 2002). Power spectral densities at steep (90°) and shallow (30°) angles to the jet axis were also calculated from the low-dimensional far-field prediction, though this failed to produce any reliable

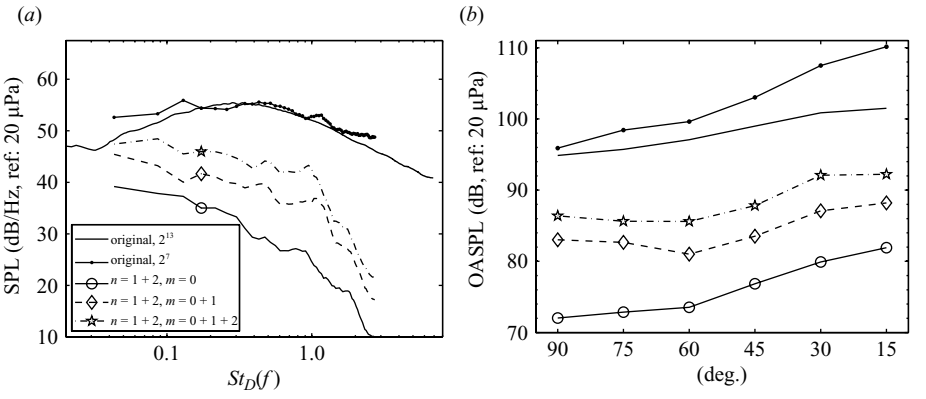

FIGURE 20. (*a*) Comparison of far-field ($r/D = 75$) power spectral densities at 60° to the jet axis. (*b*) Comparison of OASPL directivity.

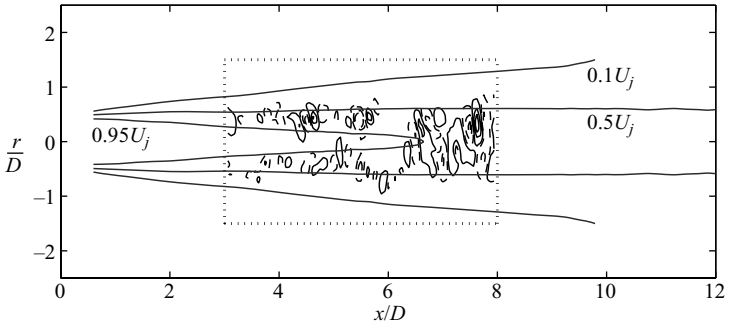

FIGURE 21. Instantaneous visualization of the Lighthill source term from the low-dimensional estimate; positive and negative fluctuations denoted by solid and dashed lines, respectively, while the box outlines the boundaries of the entire estimated region.

and physically sensible shapes; reasons for this are discussed in § 6.1. The OASPL directivity is shown in figure 20 (*b*). Aside from the small dip at 60°, the predicted trends show qualitatively good agreement with the original measurements. The numerical simulations of Freund & Colonius (2002) have investigated the effectiveness of applying these low-dimensional tools to problems in jet aeroacoustics. The current findings are qualitatively consistent with their solutions using a kinetic energy POD based norm: a preservation of the general shape of the OASPL while the energy is significantly attenuated.

6.1. *Shortcomings in the low-dimensional estimate and far-field prediction*

The prominent noise-producing region of subsonic and supersonic jet flows is restricted to the first two potential core lengths of the jet where the envelope of growth, saturation and decay is manifest (Ffowcs Williams & Kempton 1978). A number of more recent studies have thoroughly documented this behaviour. Some examples include the experimental measurements of Arakeri *et al.* (2003), Ukeiley & Ponton (2004) and Alkislar *et al.* (2007), and the direct numerical simulations of Freund (2001). In figure 21 an instantaneous visualization of the Lighthill source term from this low-dimensional estimate is illustrated alongside an outline of the mean streamwise velocity from the Mach 0.85 jet study of Ukeiley *et al.* (2007). Complementary to the spatial modes shown in figure 5, the source terms are also

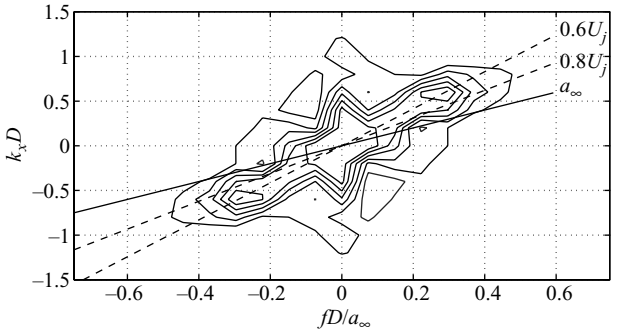

FIGURE 22. The volume averaged acoustic sources in wavenumber–frequency space.

confined to the high-speed regions of the jet flow where the convective speeds are greater than $0.6U_j$. What is most important about this illustration, however, is that the source field is confined axially to a region of space centred around the growth and early saturation regions of the jet flow. Surely an accurate prediction of the far-field pressure should include the sources of noise from regions extending beyond $x/D = 8$, irrespective of a low-dimensional representation of the flow. Ukeiley & Ponton (2004) suggest that the prominent sources of noise for this jet flow emanate from a region between $x/D = 7$ and 13.

Nevertheless, an important question to address here is whether this reduced-order estimate of a jet flow sufficiently retains the sources of noise. An analysis of the wavenumber–frequency make-up of the Lighthill source term is computed to address this question, following the discussions of Freund (2001). The definition for the volume-averaged source term in wavenumber–frequency space is as follows:

$$S_v(k_x, f) = \frac{1}{M}\sum_m \int_R S_{kf}(r; k_x, f, m) r \mathrm{d}r, \tag{6.4}$$

where the transformation from space and time to wavenumber and frequency is straightforward,

$$S_{kf}(r; k_x, f, m) = \frac{1}{2\pi}\int\int S(r, x, t; m) \mathrm{e}^{-\mathrm{i}(k_x x + 2\pi f t)} \mathrm{d}x \mathrm{d}t, \tag{6.5}$$

and the Lighthill source term is obtained from (6.3). Since radiated sound is produced from the change in the turbulent sources of noise as they convect through the flow, the analysis provides a global means by which we can qualitatively assess the retention of the sound-production mechanisms in this low-dimensional estimate. Of course, only a small fraction of these sources are efficient radiators of sound and so such an analysis is still limited in the way of pinpointing the process by which turbulent energy is converted into radiated sound.

The resulting operation is shown in figure 22, using the low-dimensional estimate comprising the first two POD modes and the first three Fourier-azimuthal modes. An assumption that $k_x, f = -k_x, -f$ has been inserted, and a 10 % bandwidth moving filter used to smooth the data. Here we can see that the source strength for this region of the flow (between $x/D = 3$ and 8) convects between $0.6U_j$ and $0.8U_j$. A line identifying the ambient sound speed has been drawn to mark the range of wavenumbers and frequencies that are efficient at radiating sound to the far field as defined by $|f/k_x| > a_\infty$. Consistent with the analysis of Freund (2001) and

Tinney & Jordan (2008), the radiated sound constitutes only a small fraction of the total source field's energy; most energy resides around pressure waves that become negligible within a few wavelengths from the jet: $|f/k_x| < a_\infty$, and with convective speeds consistent with the approximations displayed in figure 7. The strongest sources from Freund (2001) were centred around a convective Mach number of $M_c = 0.3$; M_c defined as the convection speed divided by the ambient sound speed. The strongest sources here reside around $M_c = 0.56$ (or $0.7U_j$). The discrepancies are a testament to the importance of the downstream regions after the close of the potential core where the convective speeds are much smaller and where the prominent sources of noise reside.

7. Concluding remarks

An investigation into the low-order behaviour of the velocity field, and its capacity to drive the signatures in the near-field pressure located within the periphery of the hydrodynamic region of a Mach 0.85 axisymmetric jet flow, has been presented using a purely empirical set of data. Where the sensing and estimation of the low-order flow dynamics are concerned, the spectral linear stochastic estimation procedure has demonstrated itself to be a robust and useful tool for preserving the evolution of the time scales associated with the low-order modes of the velocity field. The reduction of both the pressure field and the velocity field into coefficients that were representative of their low-order behaviours was also shown to provide the most effective means (thus far) by which the two fields could be related, when compared to former attempts (Hall *et al.* 2005; Tinney *et al.* 2005). The pressure field was shown to manifest a profound sensitivity to different components of the velocity field (expanding on the findings of Lau *et al.* 1972) even when large spatial separations, of the order of 7 jet diameters, existed between the two.

A low-dimensional estimate using only the most energetically related pressure–velocity modes identified a bursting-like event. The event occurred with a regularity coinciding with the characteristic Strouhal number of the jet and occurred throughout the near-field regions of the jet. This burst-like event was similar to the 'volcano-like' eruptions that were observed in the incompressible and lower-Reynolds-number studies of Citriniti & George (2000) and is thought to be associated with the prominent sources of noise that have been known to occur after the collapse of the potential core. Reconstructions of the full vorticity field using the Q criterion and various spatial-mode combinations provided a visual means by which the spatial-temporal behaviour of the various flow modes in the jet could be presented. The reconstructions comprised solutions to the vector POD with all three-velocity components.

Predictions of the far-field sound pressure were invoked using Lighthill's analogy from which the retarded time topologies were shown to manifest high-frequency motions at steep angles to the jet axis (90°), relative to lower-frequency motions at shallow angles to the jet axis (60° and 30°). The low-frequency motions of the source field comprised wavy patterns that followed along lines with oblique angles to the characteristic time-scale of the flow, appearing thus to be a consequence of the 'volcano-like' bursting event illustrated in the low-dimensional estimate. Estimates of the OASPL directivity agreed reasonably well with far-field measurements performed *in situ*. This work, thus constitutes a first step in developing low-dimensional models from hydrodynamic pressure signatures for estimating and predicting the behaviour of the deterministic energy-containing events that govern many of the physical constituents in turbulent flows.

There are of course many areas in which we can improve and expand on the current work. Foremost, as pressure fluctuations are known to comprise both linear and quadratic dependencies with velocity fluctuations, the linear truncation of the conditional estimate constitutes a certain level of uncertainty regarding the overall accuracy of the final estimate. While a linear estimate is clearly the simplest approach, even from a controls point of view, the quadratic terms (which we have neglected here) may provide the necessary ingredients by which we could perform a more accurate forecast of the jet's downstream regions of the flow where the dominant region of sound production is known to occur (between $x/D = 7$ and 13 for these conditions). The current estimate falls short of accurately reconstructing this region and is a contributing source of error in the far-field predictions at steep and shallow angles. We could overcome this by simply repositioning the near-field azimuthal array further downstream. Furthermore, as the POD bases are empirically derived from the turbulent kinetic energy (near-field property), the bases manifest contributions from fluctuations that are conceivably irrelevant to the far-field sound pressure. Freund & Colonius (2002) explored the sensitivity of the far-field sound pressure to contributions from different POD bases using a host of different near-field norms (fluctuating kinetic energy, pressure, streamwise velocity, sound pressure at $30D$). The objective was to identify a norm such that relatively few POD modes could represent the important mechanisms by which the bulk generation of sound is manifest. Their work constitutes an encouraging finding where POD based norms are concerned. However, experimentally, we continue to be confined by our instruments and by Reynolds numbers that are more representative of current state-of-the-art propulsion systems. To this end, a further refinement to the linear estimate of velocity fluctuations from pressure fluctuations (or vice versa) could be performed by deriving empirically, a POD basis for the velocity field that is first pressure filtered.

Tinney *et al.* (2007) demonstrated this by performing a pressure-filtered estimate of a Mach 0.60 jet flow, derived by means of raw-pressure and raw-velocity correlations, via a spectral linear stochastic estimation. Subsequently, the POD bases were determined from the estimated velocity (three-dimensional decomposition), and so the functions were an effect of the pressure-filtered velocity, not the turbulent kinetic energy. The difference being a set of functions (velocity) derived from a pressure-filtered kernel, rather than a kernel comprising the full spectrum of turbulent kinetic energy. In a similar way, Jordan *et al.* (2007) have developed a method for separating 'noisy' flow events from 'quiet' flow events. In hindsight, the results demonstrated here are similar to those of Tinney *et al.* (2007), that is, there is a preservation of only the low-order modes of the flow $m = 0, 1, 2$, where hydrodynamic pressure-filtering effects are implicit to the estimate. The experiments of Guitton *et al.* (2007) used near-field line and azimuthal arrays of pressure sampled synchronously with a three-component LDA system traversed to various positions within the potential core and shear-layer regions of a co-planar co-axial nozzle; this will provide a database by which we can expand on these low-dimensional techniques using experimental data.

Where a prediction of the far-field spectra is concerned, we can improve on our attempts by considering inadequacies in the low-dimensional estimate, the appropriateness of the analogy selected (see Freund *et al.* 2005), or the neglect of unavailable flow properties (i.e. density fluctuations). Aside from inadequacies in the low-dimensional estimate and missing flow properties, alternative analogies, specifically, the vortex-noise analogies of Powell (1964) and Möhring (1978) may be useful as they have been investigated by means of experimental work by Schram & Hirschberg (2003). Apart from the appeal of these analogies constituting a more

intuitive feel of the source mechanisms according to Jordan & Gervais (2007), they are arguably more attractive using low-dimensional flow models as these models are most efficiently described in terms of vortex dynamics. This will be among other topics for future consideration.

This work was made possible through the generous support of Syracuse University and the Air Force Office of Scientific Research. In addition, the authors would like to acknowledge Joël Delville, Laurent Cordier, Peter Jordan and Pierre Comte for many helpful discussions.

REFERENCES

Adrian R. J. 1977 On the role of conditional averages in turbulence theory. In *Turbulence in Liquids; Proc. 4th Biennal Symp. Missouri, USA* (A77-40426 18-34), *Princeton, NJ*, pp. 323–332. Science Press.

Adrian, R. J. 1991 Particle-imaging techniques for experimental fluid mechanics. *Annu. Rev. Fluid. Mech.* **23**, 261–304.

Adrian, R. J. 1996 Stochastic estimation of the structure of turbulent flows. *Eddy Structure Identification* (ed. J. P. Bonnet), pp. 145–195. Springer.

Alkislar, M. B. Krothapalli, A. & Butler, G. W. 2007 The effect of streamwise vortices on the aeroacoustics of a Mach 0.9 jet. *J. Fluid Mech.* **578**, 139–169.

Arakeri V. H., Krothapalli, A., Siddavaram, V., Alkislar, M. B. & Lourenco, L. M. 2003 On the use of microjets to suppress turbulence in a Mach 0.9 axisymmetric jet. *J. Fluid Mech.* **490**, 75–98.

Arndt, R. E. A., Long, D. F. & Glauser, M. N. 1997 The proper orthogonal decomposition of pressure fluctuations surrounding a turbulent jet, *J. Fluid Mech.* **340**, 1–33.

Aubry, N., Holmes, P., Lumley, J. & Stone, E. 1988 The dynamics of coherent structures in the wall region of a turbulent boundary layer. *J. Fluid Mech.* **192**, 115–173.

Batchelor, G. K. 1951 Pressure fluctuations in isotropic turbulence. *Proc. Camb. Phil. Soc.* **47**, 359–374.

Bendat, J. S. & Piersol, A. G. 1980 *Engineering Applications of Correlation and Spectral Analysis.* John Wiley.

Bergmann, M., Cordier. L. & Blancher, J.-P. 2005 Optimal rotary control of the cylindrical wake using proper orthogonal decomposition reduced-order model. *Phys. Fluids* **17**, 097101-1.

Berkooz, G., Holmes, P. & Lumley, J. L. 1993 The proper orthogonal decomposition in the analysis of turbulent flows. *Annu. Rev. Fluid Mech.* **25**, 539–75.

Bonnet, J.-P., Cole, D. R., Delville, J., Glauser, M. N. & Ukeiley, L. S. 1994 Stochastic estimation and proper orthogonal decomposition: complementary techniques for identifying structure. *Exps. Fluids* **17**(5), 307–314.

Borée, J. 2003 Extended proper orthogonal decomposition: a tool to analyse correlated events in turbulent flows. *Exps. Fluids* **35**, 188–192.

Bradshaw, P., Ferriss, D. H. & Johnson, R. F. 1964 Turbulence in the noise-producing region of a circular jet. *J. Fluid Mech.* **19**, 591–624.

Chakraborty, P., Balachandar, S. & Adrian, R. J. 2005 On the relationships between local vortex identification schemes. *J. Fluid Mech.* **535**, 189–214.

Chang, P. 1985 Fluctuating pressure and velocity fields in the near field of a round jet. PhD thesis, University of Illinois at Urbana-Champaign, Urbana, USA.

Chong, M. S., Perry, A. E. & Cantwell, B. J. 1990 A general classification of three-dimensional flow fields. *Phys. Fluids* A **2**, 765–777.

Citriniti, J. H. & George, W. K. 2000 Reconstruction of the global velocity field in the axisymmetric mixing layer utilizing the proper orthogonal decomposition. *J. Fluid Mech.* **418**, 137–166.

Coiffet, F., Delville, J., Ricaud, F. & Valiere, J. C. 2004 Nearfield pressure of a subsonic free jet, estimation and separation of hydrodynamic and acoustic components. *Proc. 10th European Turbulence Conf.* (ed. H. I. Anderson & P. A. Krogstad), *Trondheim, Norway*, p. 168.

Coiffet, F., Jordan, P., Delville, J., Gervais, Y. & Ricaud, F. 2006 Coherent structures in subsonic jets: a quasi-irrotational source mechanism? *Intl. J. Aeroacoust* **5**, 67–89.

Crighton, D. G. 1975 Basic principles of aerodynamic noise generation. *Prog. Aerospace Sci.* **16**, 31–96.

Druault, P., Delville, J. & Bonnet, J.-P. 2005 Experimental 3D analysis of the large scale behavior of a plane turbulent mixing layer? *Flow Turbulence Combust.* **74**, 207–233.

Elsinga, G. E., Scarano, F., Wieneke, B. & Oudheusden, B. W. 2006 Tomographic particle image velocimetry. *Expe. Fluids* **41**, 933–947.

Ewing, D. & Citriniti, J. 1999 Examination of a LSE/POD complementary technique using single and multi-time information in the axisymmetric shear layer. *Proc. IUTAM Symp. in Lynby, Denmark, 25–29 May, 1997* (ed. J. N. Sorensen, E. J. Hopfinger & N. Aubry), pp. 375–384. Kluwer.

Ffowcs Williams, L. E. & Kempton, A. J. 1978 The noise from the large scale structure of a jet. *J. Fluid Mech.* **84**, 673–694.

Freund, J. B. 2001 Noise sources in a low-Reynolds-number turbulent jet at Mach 0.9. *J. Fluid Mech.* **438**, 277–305.

Freund, J. B. & Colonius, T. 2002 POD analysis of sound generation by a turbulent jet. *AIAA Paper* 2002-0072.

Freund, J. B., Samanta, A., Wei, M. & Lele, S. 2005 The robustness of acoustic analogies. *AIAA Paper* 2005-2940.

Gamard, S., Jung, D. & George, W. K. 2004 Downstream evolution of the most energetic modes in a turbulent axisymmetric jet at high Reynolds number. Part 2. The far-field region. *J. Fluid Mech.* **514**, 205–230.

George, W. K., Beuther, P. D. & Arndt, R. E. A. 1984 Pressure spectra in turbulent free shear flows. *J. Fluid Mech.* **148**, 155–191.

Glauser, M. N. 1987 Coherent structures in the axisymmetric turbulent jet mixing layer. PhD dissertation, State University of New York at Buffalo. Amherst.

Glauser, M. N. & George, W. K. 1987 Orthogonal decomposition of the axisymmetric jet mixing layer including azimuthal dependence. *Advances in Turbulence* (ed. G. Comte-Bellot & J. Mathieu), 357–366. Springer.

Glauser, M. N., Leib, S. J. & George, W. K. 1985 Coherent structures in the axisymmetric turbulent jet mixing layer. *Proc. fifth Symp. Turb. Shear Flows, Cornell University, Ithaca, NY, USA.*

Glauser, M. N., Zheng, X. & Doering, C. 1991 The dynamics of organized structures in the axisymmetric jet mixing layer. *Trubulence and Coherent Structures* (ed. M. Lesieur & O. Metais), pp. 253–265. Kluwer.

Glauser, M. N., Young, M. J., Higuchi, H., Tinney, C. E. & Carlson, H. 2004 POD based experimental flow control on a NACA-4412 airfoil. *AIAA Paper* 2004-0575.

Gordeyev, S. V. & Thomas, F. O. 2002 Coherent structure in turbulent planar jet. Part 2. Structural topology via POD eigenmode projection. *J. Fluid Mech.* **460**, 349–380.

Grinstein, F. F., Glauser, M. N. & George, W. K. 1995 Vorticity in jets. In *Fluid Vortices* (ed. S. I. Green), pp. 65–94. Kluwer.

Guitton, A., Tinney, C. E., Jordan, P. & Delville, J. 2007 Measurements in a co-axial subsonic jet. *AIAA Paper* 2007-0015.

Hall, A. M., Glauser, M. N. & Tinney, C. E. 2005 Experimental investigation of the pressure–velocity correlation of a $M = 0.6$ axisymmetric jet. *AIAA Paper* 2005-5294.

Hall, J. W. & Ewing, D. 2006 A combined spatial and temporal decomposition of the coherent structures in the three-dimensional wall jet. *AIAA Paper* 2006-0308.

Hileman, J. I., Thurow, B. S., Caraballo, E. J. & Samimy, M. 2005 Large-scale structure evolution and sound emission in high-speed jets: real-time visualization with simultaneous acoustic measurements. *J. Fluid Mech.* **544**, 277–307.

Hudy, L. M., Naguib, A. & Humphreys, W. M. 2007 Stochastic estimation of a separated-flow field using wall-pressure-array measurements. *Phys. Fluids.* **19** (2), 024103.

Hunt, J. C. R., Wray, A. A. & Moin, P. 1988 Eddies, stream, and convergence zones in turbulent flows. *Center for Turbulence Res. Rep. CTR-S88*, 193–208.

Hussain, A. K. M. F. & Clark, A. R. 1981 On the coherent structure of the axisymmetric mixing layer: a flow-visualization study. *J. Fluid Mech.* **104**, 263–294.

Iqbal, M. O. & Thomas, F. O. 2007 Coherent structures in a turbulent jet via a vector implementation of the proper orthogonal decomposition. *J. Fluid Mech.* **571**, 281–326.

Jeong, J. & Hussain, F. 1995 On the identification of a vortex. *J. Fluid Mech.* **285**, 69–94.

Jordan, P. & Gervais, Y. 2007 Subsonic jet aeroacoustic: associating experiment, modelling and simulation. *Exps. Fluids* **44** (1), 1–21.

Jordan, P., Schlegel, M., Stalnov, O., Noack, B. R. & Tinney, C. E. 2007 Identifying noisy and quiet modes in a jet. *AIAA Paper* 2007-3602.

Jung, D., Gamard, S. & George, W. K. 2004 Downstream evolution of the most energetic modes in a turbulent axisymmetric jet at high Reynolds number. Part 1. The near-field region. *J. Fluid Mech.* **514**, 173–204.

Kerhervé, F., Jordan, P., Gervais, Y., Valière, J. C. & Braud, P. 2004 Two-point laser Doppler velocimetry measurements in a Mach 1.2 cold supersonic jet for statistical aeroacoustic source model. *Exps. Fluids* **37** (3), 419–437.

Ko, N. W. M. & Davies, P. O. A. L. 1971 The near field within the potential cone of subsonic cold jets. *J. Fluid Mech.* **50**, 49–78.

Lau, J. C., Fisher, M. J. & Fuchs, H. V. 1972 The intrinsic structure of turbulent jets. *J. Sound Vib.* **22** (4), 379–406.

Lau, J. C., Morris, P. J. & Fisher, M. J. 1979 Measurements in subsonic and supersonic free jets using a laser velocimeter. *J. Fluid Mech.* **93**, 1–27.

Laufer, J. & Yen, T. C. 1983 Noise generation by a Low Mach number jet. *J. Fluid Mech.* **134**, 1–31.

Lighthill, M. J. 1952 On sound generated aerodynamically: general theory. *Proc. R. Soc. Lond.* **211**, 564–587.

Lumley, J. L. 1967 The structure of inhomogenous turbulent flows. In *Atmospheric Turbulence and Radio Wave Propagation* (ed. A. M. Yaglom & V. I. Tatarski), pp. 166–178. Nauka, Moscow.

Lumley, J. L. 1981 Coherent structure in turbulence. In *Transition and Turbulence* (ed. R. E. Meyer), p. 215. Academic.

Mankbadi, R. & Liu, J. T. C. 1984 Sound generated aerodynamically revisited: large-scale structures in a turbulent jet as a source of sound. *Phil. Trans. R. Soc. Lond.* A **311**, 183–217.

Michalke, A. & Fuchs, H. V. 1975 On turbulence and noise of an axisymmetric shear layer. *J. Fluid Mech.* **70**, 179–205.

Möhring, W. 1978 On vortex sound at low Mach number. *J. Fluid Mech.* **85**, 685–691.

Murray, N. E. & Ukeiley, L. S. 2006 Flow field dynamics in open cavity flows. *AIAA Paper* 2006-2428, 1–16.

Noack, B. R., Afanasiev, K., Morzynski, M. & Thiele, F. 1993 A hierarchy of low-dimensional models for the transient and post-transient cylinder wake. *J. Fluid Mech.* **497**, 335–363.

Pan, G. & Meng, H. 2002 Digital holographic PIV for 3D flow measurement. *ASME Paper* 2002-33173.

Perret, L., Collin, E. & Delville, J. 2006 Polynomial identification of POD based low-order dynamical systems. *J. Turbulence* **7**, 1–15.

Petersen, R. A. 1978 Influence of wave dispersion on vortex pairing in a jet. *J. Fluid Mech.* **89**, 469–495.

Picard, C. & Delville, J. 2000 Pressure velocity coupling in a subsonic round jet. *Intl J. Heat Fluid Flow* **21**, 359–364.

Pinier, J. T., Ausseur, J. M., Glauser, M. N. & Higuchi, H. 2007 Proportional closed-loop feedback control of flow separation. *AIAA J.* **45** (1), 181–190.

Powell, A. 1964 Theory of vortex sound. *J. Acoust. Soc. Am.* **36**, 177–195.

Powell, A. 1998 *Aerodynamic and Jet Noise*. John Wiley.

Pu, Y., Song, X., Meng, H. 2000 Off-axis holographic particle image velocimetry for diagnosing particulate flows. *Exps. Fluids* **29** (7), 117–128.

Raffel, M., Willert, C. & Kompenhans, J. 1998 *Particle Image Velocimetry*. Springer.

Rempfer, D. 2000 On low-dimensional Galerkin models for fluid flow. *Theor. Comput. Fluid Dyn.* **14**, 75–88.

Ribner, H. S. 1969 Quadrupole correlations governing the pattern of jet noise. *J. Fluid Mech.* **38** (1), 1–24.

Rowley, C. W., Colonius, T. & Murray, R. M. 2004 Model reduction for compressible flows using POD and Galerkin projection. *Physica* D **189**(1–2), 115–129.

Schram, C. & Hirschberg, A. 2003 Application of vortex sound theory to vortex-pairing noise: sensitivity to errors in flow data. *J. Sound Vib.* **266**, 1079–1098.

Taylor, J. A. & Glauser, M. N. 2004 Towards practical flow sensing and control via POD and LSE based low-dimensional tools. *Trans. ASME* I: *J. Fluids Engng* **126**, 337–345.

Taylor, J. T., Ukeiley, L. S. & Glauser, M. N. 2001 A low-dimensional description of the compressible axisymmetric shear layer. *AIAA Paper* 2001-0292, 1–10.

Tinney, C. E. 2005 Low-dimensional techniques for sound source identification in high speed jets. PhD dissertation, Syracuse University, Syracuse.

Tinney, C. E. & Jordan, P. 2008 The near-field pressure surrounding co-axial subsonic jets. *J. Fluid Mech.* **611**, 175–204.

Tinney, C. E., Taylor, J. A., Eaton, E. & Glauser, M. N. 2002 Low dimensional descriptions of axisymmetric flows. *Proc. 9th European Turbulence Conf. Southampton, UK* (ed. I. P. Castro & P. E. Hancock).

Tinney, C. E., Hall, A., Glauser, M. N., Ukeiley, L. S. & Coughlin, T. 2004 Designing an anechoic chamber for the experimental study of high speed heated jets. *AIAA Paper* 2004-0010.

Tinney, C. E., Glauser, M. N. & Ukeiley, L. S. 2005 The evolution of the most energetic modes in a high subsonic Mach number turbulent jet. *AIAA Paper* 2005-0417.

Tinney, C., Coiffet, F., Delville, J., Glauser, M., Jordan, P & Hall, A. 2006 On spectral linear stochastic estimation. *Exps. Fluids* **41** (5), 763–775.

Tinney, C. E., Jordan, P., Delville, J., Hall, A. M. & Glauser, M. N. 2007 A time-resolved estimate of the turbulence and sound source mechanisms in a subsonic jet flow. *J. Turbulence* **8** (7), 1–20.

Tinney, C. E., Glauser, M. N. & Ukeiley, L. S. 2008 Low-dimensional characteristics of a transonic jet. Part 1. Proper orthogonal decomposition. *J. Fluid Mech.* **612**, 107–141.

Townsend, A. A. 1976 *The Structure of Turbulent Shear Flow*, 2nd edn. Cambridge University Press.

Ukeiley, L. S. & Murray, N. E. 2007 Modified quadratic stochastic estimation of resonating subsonic cavity flow. *J. Turbulence* **8**, p. 53.

Ukeiley, L. S. & Ponton, M. K. 2004 On the near field pressure of a transonic axisymmetric jet. *Intl. J. Aeroacoust.* **3** (1), 43–66.

Ukeiley, L. S., Cole, D. R. & Glauser, M. N. 1993 An examination of the axisymmetric jet mixing layer using coherent structure detection techniques. *Eddy Structure Identification in Free Turbulent Shear Flows., Proc. of the IUTAM Symp.-Poitiers October 1992* (ed. J.-P. Bonnet & M. N. Glauser), 550–534. Kluwer.

Ukeiley, L., Seiner, J. & Ponton, M. 1999 Azimuthal structure of an axisymmetric jet mixing layer. *ASME Paper* FEDSM 1999-7252.

Ukeiley, L., Cordier, L., Manceau, R., Delville, J., Glauser, M. N. & Bonnet, J. P. 2001 Examination of large scale structures in a turbulent plane mixing layer. Part 2. Dynamical systems model. *J. Fluid Mech.* **441**, 67–108.

Ukeiley, L. S., Tinney, C. E., Mann, R. & Glauser, M. N. 2007 Spatial correlations in a transonic jet. *AIAA J.* **45** (6), 1357–1369.

Viswanathan, K. 2004 Aeroacoustics of hot jets. *J. Fluid Mech.* **516**, 39–82.

Wernet, M. P. 2006 Time resolved PIV for space–time correlations in hot jets. *AIAA Paper* 2006-0047.

Yule, A. J. 1978 Large-scale structure in the mixing layer of a round jet. *J. Fluid Mech.* **89**, 413–432.

Zhou, J., Adrian, R. J., Balachandar, S. & Kendall, T. M. 1999 Mechanisms for generating coherent packets of hairpin vortices. *J. Fluid Mech.* **387**, 353–396.